Monitoring the Behaviour of a Battery-free Water Powered Sensor

by

Simran Elizabeth Chathanat

A thesis

presented to the University of Waterloo

in fulfillment of the

thesis requirement for the degree of

Master of Applied Science

in

Mechanical and Mechatronics Engineering

Waterloo, Ontario, Canada, 2023

© Simran Elizabeth Chathanat 2023

Author's Declaration

I hereby declare that I am the sole author of this thesis. This is a true copy of the thesis, including any required final revisions, as accepted by my examiners.

I understand that my thesis may be made electronically available to the public.

Abstract

The Insurance Bureau of Canada says, “Water is the new fire”. In terms of cost of damage to homeowners and insurers, water damage is a rapidly growing threat to property and can have insidious, long-term effects if not detected early [1]. In a study from 2018, water leaks from multiple sources are shown to be devastating to buildings [2]. Water leaks cause a few major issues such as structural damage, mold growth, water waste. Each of these issues is minimized when water leaks are detected promptly. Water leak detectors are important devices used to detect and alert individuals or property owners about the presence of water leaks. They play a crucial role in mitigating potential water damage, reducing water waste, and minimizing associated financial losses [3].

The work herein considers a battery-free, materials-based water leak sensor. This specific sensor is unique because to date, it is the only battery-free, Bluetooth-enabled IoT sensor ready for market [4]. A working prototype was developed in our lab, however for this sensor to work practically, the materials must be characterized and the effect of material change on electrical output must be determined.

Since the plurality of water leak sensors available for purchase are based on closing an open electrical circuit with a conductive liquid such as water, they have wide ranges of operating temperature, humidity, and other environmental conditions [2]. However, in the self-powered materials-based sensor, the materials themselves may react differently in different temperatures and humidity conditions. Additionally, this sensor depends heavily on a pressed-powder palette, a conductive, porous material that absorbs water. This palette is essential to the function of the sensor however, its participation in the power generation reaction is not well known.

The following thesis, therefore, explores three main subjects in relation to the sensor: 1) the role of palette in the sensor and how it changes in aging conditions, 2) the sensitivity of the sensing materials to high temperature and humidity conditions, and finally 3) a proposed improvement to this pressed powder palette.

Acknowledgements

First, I have to thank my supervisor, Professor Norman Zhou, for giving the opportunity to work on the self-powered water leak sensor project. Professor Zhou always gave me the freedom to follow my research interests. His encouragement brought out many of my strengths in the last two years and his guidance has been invaluable.

I would also like to thank Professor George Shaker who frequently collaborated on this project. I enjoyed my time working with him and his team and learned more about electronics than I ever realized I would.

I especially would like to acknowledge my colleagues, Kamalpreet Kaur, Mohammadreza Rouhi, and Xiaoye Zhao with whom I have spent countless hours in meetings and in phone calls testing the strength of our ideas, and in the end with whom I got to complete great work. I am very grateful for the time I got to spend with you all.

Completing this degree took much more than academic support and so I would like to acknowledge my parents who I talked to nearly daily. I would also like to acknowledge my friends in Waterloo: Claire, Alyssa, Adrianna, Hala, and Luka who were always around to uncoil me when I was anxious.

Dedication

To my parents, Henrics and MaryAnn Chathanat and my dog, Rajma. Countless afternoons spent running around the backyard always brought the light back into my life.

And to all my teachers who allowed my quiet questions to bubble into relentless curiosity.

Table of Contents

Author's Declaration ii

Abstract iii

Acknowledgements v

Dedication vi

List of Figures x

List of Tables xiii

Chapter 1 Introduction 1

1.1 Background 1

1.2 Water Leak Detectors 2

1.3 Problem Statement 4

1.4 Objective 5

1.5 Thesis Outline 5

Chapter 2 Literature Review 6

2.1 Chapter 2 Introduction 6

2.2 Water Leaks and Detection Technologies 6

2.3 IoT Devices and the Case for Embedded Energy Harvesters 8

2.3.1 Energy Harvesting Technologies 10

2.4 Redox Reactions and Metal-Air Electrochemistry 12

2.4.1 Metal-Air Cells 14

2.5 Aqueous Magnesium Electrochemical Cells 17

2.6 Graphite Oxidation and Power Generation Applications 19

2.7 Self-powered Water Leak Detector Prototype 20

2.8 Summary 21

Chapter 3 Experimental Methodology and Characterization Methods 22
3.1 Sample Preparation and Sensor Components 22
3.1.1 Sensor Materials 23
3.1.2 Assembling sensor unit 23
3.2 Characterization Methods 24
3.2.1 SEM and EDX 24
3.2.2 XPS 25
3.2.3 Raman 26
3.3 Test Set-up for Electrical Measurements 27
3.3.1 Experimental methodology 27
3.3.2 Sensor Behaviour at Standard Conditions 28
3.4 Summary 29
Chapter 4 Role of Graphite in the Sensor 30
4.1 Introduction 30
4.2 Sample Conditions 30
4.3 Graphite Hydrophobicity 31
4.4 SEM Particle Analysis on Graphite 33
4.5 EDX Elemental Analysis on Graphite 34
4.6 XPS 39
4.7 Raman 43
4.8 Summary 47
Chapter 5 Effect of Environmental Conditions on Sensor Function 48
5.1 Introduction 48
5.2 Temperature Effects 48

5.2.1 Materials Only Test 49
5.2.2 In Package Test 50
5.3 Humidity Effects 52
5.4 Aging and Lifetime Testing 57
5.4.1 Accelerated Aging Testing 57
5.5 Shelf Life: Long Term Viability of Materials Based Water Leak Sensor 59
5.5.1 Sensor Voltage Mapped with Monthly Absolute Humidity 60
5.6 Summary 62
Chapter 6 63
Development of a Graphite Composite for Improved Sensor Resilience 63
6.1 Introduction 63
6.1.1 PVAc - Graphite Composite: Response Variables 64
6.2 Statistical Analysis of Response Variables 65
6.2.1 Design of Experiments 66
6.2.2 One Way ANOVA 67
6.2.3 Maximum Voltage 67
6.2.4 Power Generation 70
6.2.5 Voltage Decay 72
6.3 Optimization of Graphite Composite Factors 74
6.4 Summary 75
Chapter 7 Conclusions and Recommendations 76
7.1 Conclusions 76
7.2 Recommendations 78
References 79

List of Figures

Fig. 1: Self-powered water leak sensor full system including essential elements such as the sensor, gateway, cloud backend, and user interface. 3
Fig. 2: Power Generation Material Stack. The materials stack consists of pressed graphite powder, filter paper and magnesium disk. 4
Fig. 3 Holistic approach to water leak detection including pipe flow sensors, rope sensor and point leak detectors adapted from [9] 7
Fig. 4 a) Moen flow, pipe leak sensor with water auto-shutoff [29], b) Pillar's multi-IoT-sensor site monitoring box [30], D-link point and rope sensor [31] 9
Fig. 5 a) Standard Reduction Potential Table [47], b) Zinc-copper electrochemical voltaic cell [48]. 13
Fig. 6 Theoretical Energy Densities for Different Metal-Air Batteries [58] 15
Fig. 7 a) Schematic of metal-air battery from Park 2015[59], b) Schematic configuration and operation principle for aqueous metal−air batteries from Li 2017. The oxygen reduction reaction taking place at the porous air cathode is displayed in the inset. [58] 16
Fig. 8 a) Magnesium water coin cell [68], Polyaniline foam scaffold for cathodic reductin in aqueous magnesium battery [69] 18
Fig. 9 a) Flake graphite has a layered structure constituting carbon atoms in a hexagonal lattice [73], b) The graphene oxide molecular structure consists of carbon, hydrogen and oxygen [74]. 19
Fig. 10 Schematic of the Mg−CNF device used for water detection, as well as the Mg−water reactions and ion transportation happening in the CNF porous structure [63]. 21
Fig. 11 a) Blown up render of the self-powered water leak detector in this work including both the sensor unit and electronics [18] b) Components of leak detector [18] 22
Fig. 12 a) Instron tensile tester used for pressing graphite, b) graphite press mold, c) open sensor package without materials, d) magnesium sheet before and after sanding, e) filter paper pieces 24
Fig. 13 a) SEM and EDX Instrument;, b) XPS Instrument; (c) Raman 26
Fig. 14 a) Experimental set-up for the in-package test without electronic unit, b) schematic of materials only test setup 28
Fig. 15 Standard load test results at 25°C, n=8. Inset shows higher resolution of peak voltage. 29
Fig. 16 a) Hydrophilic nature of graphite palette and b) after one drying cycle, graphite is noticeably hydrophobic 31
Fig. 17: Image of graphite particles at a) 500x magnification using SE1: b) 5.00kV, c) 20.00kV 33

Fig. 18: EDX for graphite. a) SEM image of graphite for Spectrum 141, b) SEM image of graphite for Spectrum 141, c) EDX of graphite for Spectrum 136, d) EDX of graphite for Spectrum 136.....35
Fig. 19: Boxplots of the EDX oxygen content across 4 conditions. The measure of central tendency is the mean. Standard deviations are plotted as 'x'.....37
Fig. 20 a,b) Low resolution XPS spectrum sweep for DG sample and MS5 sample, c,d) High resolution XPS spectrum from 40 to 60 eV to determine magnesium content in DG sample, and MG5 sample. 40
Fig. 21 a,b) Low resolution XPS spectrum sweep for DG sample and MS5 sample, c,d) High resolution XPS spectrum from 40 to 60 eV to determine magnesium content in DG sample, and MG5 sample. 42
Fig. 22: Raman Spectra overlay for graphite samples in 4 conditions: DG, GS, MS, MS5 44
Fig. 23: Raman bands a) D band locations, b) G band locations, c) G' band locations 45
Fig. 24 a) Average load test voltage characteristic (n=5) for materials only samples over each temperature. b) Average maximum voltage plotted against temperature. 50
Fig. 25: a) Average load test voltage characteristic (n=5) for materials only samples over each temperature. b) Average maximum voltage plotted against temperature. 51
Fig. 26: Humidity chamber setup for retaining 85% humdity 52
Fig. 27: Results for the humidity test for materials only samples: (a) reference at 25°C, (b) Voltage after 5 days, (c) Voltage after 10 days, (d) Voltage after 15 days 54
Fig. 28: Results for the humidity test for in-package samples: (a) reference at 25°C, (b) Voltage after 5 days, (c) Voltage after 10 days, (d) Voltage after 15 days.....56
Fig. 29 : Average power output after exposure to high temperature condition over 28 days.....58
Fig. 30: Shelf Life 1 month (July 2021 vs February 2023). In July 2021, the behaviour of the fresh sensors is much closer to fresh sensors, there is a visible difference.....60
Fig. 31: a) Average power of packaged shelf life samples over 16 months, b) average power of shelf-life samples over 16 months, plotted with monthly absolute humidity. 61
Fig. 32: Example raw data with a) maximum voltage, b) average power over 150s, c) voltage decay64
Fig. 33 Max. Voltage scatterplots with best fit curves.....68
Fig. 34: Max. Voltage: a) ANOVA table, b) Regression table, c) surface plot, d) contour plot 69
Fig. 35: Power scatterplots with best fit curves 70
Fig. 36: Power: a) ANOVA table, b) Regression table, c) surface plot, d) contour plot 71

Fig. 37: Voltage Decay scatterplots with best fit curves.....72
Fig. 38: Voltage Decay a) ANOVA table, b) Regression table, c) surface plot, d) contour plot.....73
Fig. 39: Minitab optimization tool indicates what compression and graphite percentage would produce optimized maximum voltage, power output and voltage decay.....74

List of Tables

Table 1: Water Leak Sensors on the Market: Sensing Tasks and Operating Conditions 8
Table 2: Energy Harvesting Sources with Theoretical Power Density 11
Table 3: Composition of AZ31b by Weight 17
Table 4: Oxygen and Carbon Content in Graphite Samples Under 4 Conditions 36
Table 5: Raman peak locations 46
Table 6: Equipment Models and Accuracy 65
Table 7: Coded Parameters for CCD and Real Values 66

Chapter 1
Introduction

1.1 Background

Our world is defined by our interactions with water. From large scale landscape erosion to being a key biological molecule, water is a force of nature that we both aim to harness and endure. On an everyday scale, we need water to survive, and must protect ourselves from the effects of water damage which is often irreversible to structures and devices. Water is ubiquitous and available, so the idea of using water as a source of energy is incredibly attractive [1],[2].

Water damage is a huge liability to building materials such as wood, drywall, and concrete. It causes these materials to swell, warp, crumble, and grow mold [3], [4], [5]. Ultimately it becomes necessary to repair or replace these materials. Considering the sheer number of buildings in North America that experience water damage in any given year – 1.6% of the over 150 million buildings – addressing this damage is a huge draw on natural resources [4], [5]. The size of insurance claims to cover water damage for the average homeowner has been estimated at 5000 to 7000 USD [3]. The proper maintenance of these structures can save raw materials, energy, and construction costs, and can extend the service lives of buildings. Often, water sealants and vapour barriers are deployed but are fallible and have effectiveness lifetimes [4], [5], [6]. Since water damage is insidious and can cause massive structural problems and health problems, it is imperative to monitor water leaks and detect them as early as possible, regardless of the attempts to prevent them in the first place [7], [8]. Water leak detectors in individual homes can lead to large scale efficiencies and minimize inefficiencies associated with water damage [5].

1.2 Water Leak Detectors

There are myriad water leak detectors available on the market in 2023. These sensors work on the concept of a droplet of water closing a small opening in the sensing circuitry in a variety of configurations [8], [10-17]. These sensors are either powered by wall outlets or batteries and have major limitations. First, the sensors' placement is limited by either the location of wall outlets or easy-to-reach areas where replacing or recharging the battery is not a hindrance. In the case of battery powered sensors, the inconvenience and labour involved in replacing or charging the battery limits the number of sensors that the average customer may be willing to place, especially for larger scale industrial applications. The main purpose of these sensors is to protect users from the expense and inconvenience of addressing water damage and so these problems need to be addressed.

The water leak detection system developed and discussed in this work addresses the issues with powered water leak detectors. This sensor was developed on a multidisciplinary team since the development required mechanical, materials, electrical, and cloud expertise. The system in its entirety is summarized in Fig. 1. The focus of this thesis is on the essential leak sensing mechanism itself. This sensor has also been described in literature [18], [19].

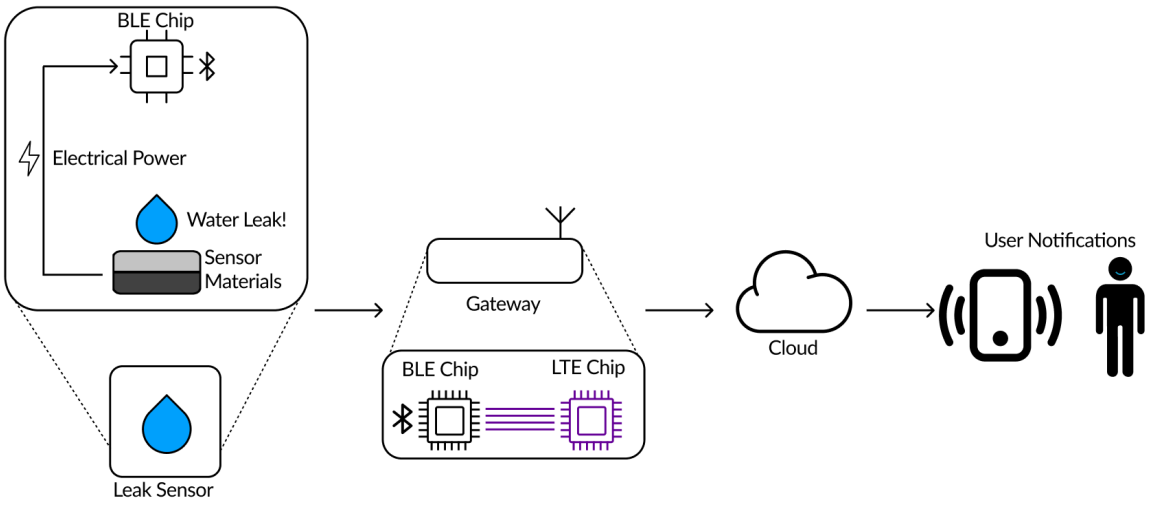


Fig. 1: Self-powered water leak sensor full system including essential elements such as the sensor, gateway, cloud backend, and user interface.

The system extracts electrical power through a reaction involving water. There are two distinct material layers (Fig. 2) that are involved in the power generation: the reactive layer and the water absorbent layer. These two parts are separated by an insulating layer to prevent short circuitry. The water contacts both materials to generate power across a load [19], [20]. The reactive layer was studied in a previous work [19], so this work focusses on characterizing and understanding the absorbent layer. Multiple materials may be used to create this system [20], however in this work, one specific system is studied.

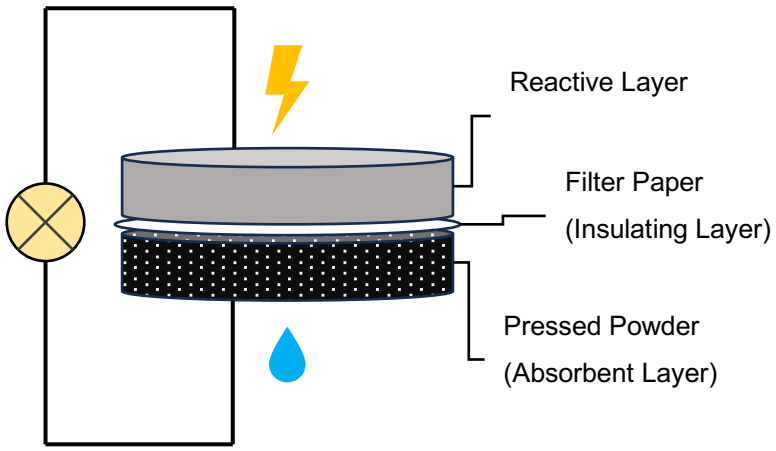


Fig. 2: Power Generation Material Stack. The materials stack consists of the main reactive later, filter paper and a pressed-powder absorbent layer.

1.3 Problem Statement

The average water leak sensor on the market depends on water to close a circuit. This type of sensor is well-known and works reliably. On the other hand, the materials-based sensor described in this thesis is dependent on a materials system. The effect of the sensor function on the materials within the sensor is unknown. Additionally, this system has unknown sensitivity to environmental conditions and aging. The materials-based, self-powered sensor in this work has advantages when compared to battery-powered sensors, however, its behaviour is more susceptible to change due to environmental conditions. These unknown behaviours must be characterized in order to form a true comparison between this battery-free sensor and powered sensors. These comparisons may be used to increase the reliability of the sensor and will guide the development and improvement of the overall system.

1.4 Objective

The objective of this thesis is to glean information about an existing prototype of a self-powered water leak sensor system. Since the sensor is powered by a reaction between its sensing materials and water from the environment, it is susceptible to the environment, unlike the typical powered sensors on the market. Therefore, more close study to the components and behaviours of the sensor are required. The main goals of this work are to first understand the role of graphite in the sensor, then and finally, evaluate the creation of a graphite composite as a replacement for the brittle graphite piece that has been used in the sensor.

1.5 Thesis Outline

The main content of this thesis is as follows: Chapter 2 is an in-depth literature review that includes water leaks and the motivation for water leak detectors, energy-harvesting systems, and the chemistry essential to understanding the self-powered water leak detector and the methods of testing included in this work. Chapter 3 is an overview of the process involved in manufacturing sensor samples, the primary testing methods and the characterization methods used in this work. Chapter 4 explores the role of graphite in the sensor by analyzing the characterization of graphite using SEM, EDX, XPS, and Raman analysis before and after the graphite is exposed to water in the functioning sensor. Chapter 5 determines the effect of conditions such as temperature changes, elevated humidity, electrolyte concentration, and overall aging on both the sensing materials and the overall sensor. Chapter 6 offers a replacement of the graphite palette with a more robust graphite composite and evaluates the performance of this composite in regards to the maximum voltage, power output and voltage decay of the sensor. Finally, Chapter 7 summarizes the overall conclusions of this work and offers recommendations for how to further our understanding of the sensing materials as well as directions for future sensor development.

Chapter 2
Literature Review

2.1 Chapter 2 Introduction

The focal point of this work is the materials stack. This stack both detects water and powers the notification system of the sensor, eliminating the need for battery power and external power. In order to characterize the behaviour of the materials stack, understand the and finally, propose improvements, it is first essential to understand the mechanism of water leak detection in the context. This chapter will first frame the landscape of water leak detectors on the market, then describe the electrochemical foundations for the technology used in the sensor. Finally, it will explain in depth the functions of the two fundamental materials in the sensor, magnesium, and graphite.

2.2 Water Leaks and Detection Technologies

More and more of us are familiar with water leaks and water damage in homes. As coastal areas continue to be plagued by rising sea levels, the occurrences of water leaks continue to increase [5]. Many structures will be ravaged, but for the ones that survive, minimizing water damage is essential. Water leaks in buildings pose significant risks and can lead to extensive damage if left unaddressed [4], [5]. These leaks can originate from various sources, such as plumbing systems, roofs, or faulty infrastructure. The consequences include structural deterioration, mold growth, and compromised electrical systems. Water damage can cause discoloration, peeling paint, and sagging ceilings. Besides the physical damage, water leaks are a huge financial burden in utility bills, construction costs, time loss and potential health hazards due to mold. Timely detection and repair are crucial to mitigate the impact of water leaks, safeguarding the integrity and safety of buildings and their occupants [5], [7], [9].

There are multiple types of water leak detectors that serve multiple purposes. Three prominent categories of water leak detectors are point detectors, rope detectors and pipe flow detectors. Each of these detector types is useful for different purposes and can be used cooperatively (Fig. 3).

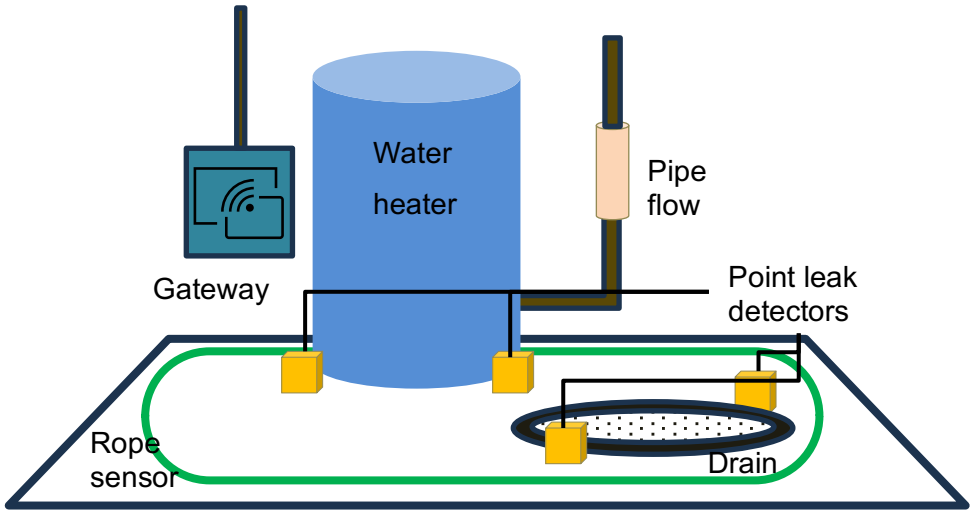


Fig. 3 Holistic approach to water leak detection including pipe flow sensors, rope sensor and point leak detectors adapted from [9]

One of the most essential problems with point leak detection is sensor placement. This is limited by multiple factors. A basic problem with which limits sensor placement is the power source of the sensor. Sensors need to be within reach of an electrical socket in the case of plug-in sensors. In the case of battery powered sensors, they still need to be within easy reach, since batteries discharge, rendering the sensor useless without replacing the battery. Many water leak sensors are available on the market and some of the most popular ones are included in Table 1 [8]. These sensors have multiple purposes an Apart from the self-powered sensor in this work, these sensors are entirely powered wither by battery powered units or plug-in units [10-17].

Table 1: Water Leak Sensors on the Market: Sensing Tasks and Operating Conditions

Name	Measurements	Operating Temperature (°C)	Lifetime (years)	Minimum Water Depth (mm)	Response Time (s)
Aqua Sensing	Water Leaks	-18 to 60	N/A	0.2	30
Flo [13]	Water Leaks, Humidity, Temp.	-29 to 60	2	< 1	2
D-Link [10]	Water Leaks	0 to 40	1.5	< 1	2
Honeywell [15]	Water Leaks, Humidity, Temp.	0 to 60	3	< 1	60
Nowa [11]	Water Leaks	0 to 49	10	0.4	2

2.3 IoT Devices and the Case for Embedded Energy Harvesters

The Internet of Things (IoT) and Wireless Sensor Networks (WSN) are rapidly growing fields as gathering and connecting data from our lives and environments becomes increasingly normalized. In a 2023 report, it was determined that the number of IoT devices grew by 18% in 2022 and it was forecasted that the total number of devices would reach 17.7 billion in 2023 [20]. The IoT is a network of devices and sensors that are connected through software and data analysis and bring together many individual technologies [21].

Sensors are a fundamental part of IoT. They extract environmental data within certain limits and are applicable in medical care, industrial monitoring, agriculture, and many other essential fields. The sensors can provide data about physical conditions such as temperature, acceleration, or gyroscopic sensors or mimic human senses, such as sound sensors, touch pressure sensors, or imaging sensors [22 - 28]. The variety of available sensor applications allows IoT to be universally useful across many fields. In some networks, it is useful to have many point nodes, whereas others have more wide-ranging sensors [28], [29]. For example, in the problem of water leaks, there are multiple detection solutions that apply to different scenarios. The different applications of water leak sensors are pictured in Fig. 4. In the case where the leaks are caused by pipes, a few flow sensors can be used to monitor leaks since pipes are already connected. In the case where leaks are caused by defects in the building envelope or condensation, point leak detectors are required [3], [9], [23]. In this case, in order to effectively cover an area of a building, many more sensors are required since the water leak detection radius of these sensors is limited. The sensor distribution determines the area or volume that is vulnerable to damage before a leak is detected.

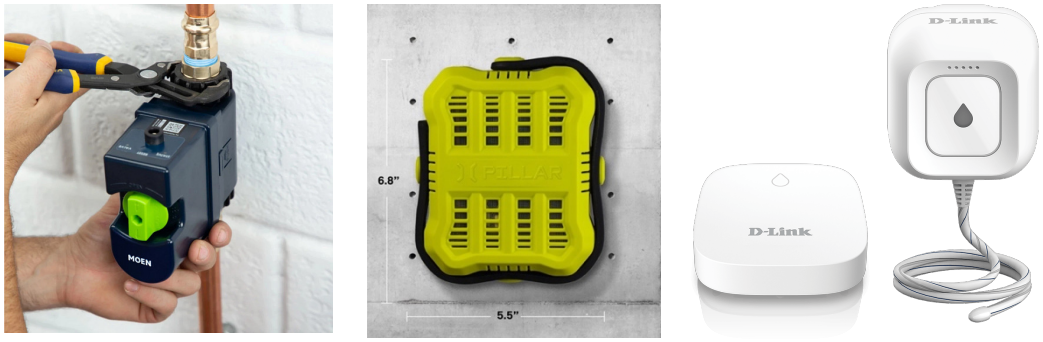


Fig. 4 a) Moen flow, pipe leak sensor with water auto-shutoff [29], b) Pillar's multi-IoT-sensor site monitoring box [30], D-link point and rope sensor [31]

The sensors that make up these networks typically use batteries. Many of these devices are relatively small, and untethered so batteries appear to be an ideal candidate to power these devices [10-17]. However, this reliance leads to a few problems. First, it makes us beholden to their battery life. The severity of this problem depends on the number of sensors and complexity of the system. For wearables, creating rechargeable battery units is relatively simple [9], [20]. Considering an IoT network in a building with hundreds of sensors collecting data is more overwhelming. The frequency of battery replacement or charging and labour involved is inconvenient. Second, in the EnABLES 2021 report, it is estimated that 78 million batteries for IoT devices will be disposed daily by 2025[30]. These two issues - the problem of the inconvenience of replacing or charging batteries and the problem of disposing of these batteries – increase dramatically as the scale of IoT projects continues to grow. As a result, in many of these applications, there is a turn towards energy harvesting or self-powered sensors [20].

2.3.1 Energy Harvesting Technologies

In order to mitigate the problems associated with powering billions of devices with batteries, energy harvesting, and smart devices are a promising alternative [30]. Energy harvesting is a wide-branching classification, but in general is the process of extracting electrical power from incidental environmental factors. Piezoelectric harvesters are a fitting representation of this definition. They use piezoelectric materials to convert stress or strain into electrical energy. This type of harvester can respond to ambient mechanical vibrations from many sources. Piezoelectric harvesters also produce characteristically low power which is common for energy harvesters. Since many energy harvesting technologies are relatively low power, they work well when integrated into small-to-miniaturized devices [25], [31].

While energy harvesting devices often can replace batteries, the adoption of energy harvesting does not necessarily end the use of batteries all together. In these embedded

systems, typically some kind of electricity storage like a capacitor or rechargeable battery. The main advantage is not being limited by having to charge or replace a battery. The main categories of energy harvesters are the technologies that drive the power generation. As described above, however, energy harvesters with one specific harvesting technology can still be used across a wide range of applications [32], [33]. Additionally, these harvesting technologies can be categorized as predictable or unpredictable, and controllable or uncontrollable. Predictability refers to whether the energy output and frequency can be modelled, and controllability refers to whether the environmental driver of energy production can be intentionally induced [34]. Some energy harvesting technologies are organized in Table 2 with their power density, predictability, and controllability.

Table 2: Energy Harvesting Sources with Theoretical Power Density

Energy Source	**Theoretical Power Density**	**Predictability**	**Controllability**	**References**
Flow	1μW/cm^3	Predictable	Non-controllable	[34], [35], [36]
Vibration	100-200μW	Unpredictable	Controllable	[34], [35], [37]
Mechanical Pressure	0.003-0.96 μW/cm^3	Unpredictable	Controllable	[34], [35], [38]
Piezoelectric Effect	330 μW/cm^3	Unpredictable	Controllable	[34], [35], [39]
RF	1 μW/cm^3	Predictable	Controllable	[34], [35], [40]
Thermal	40 μW/cm^3	Unpredictable	Controllable	[34], [35], [41]
Solar	15 mW/cm^3	Predictable	Non-controllable	[34], [35], [42]
Water electrochemistry	1-4 μW/cm^3	Unpredictable	Non-controllable	[34], [35], [43]

In the case of point water leak detectors using water contact as the main source of energy means that the energy source is both unpredictable and non-controllable. This ties the function of this sensor to the limited power supply. In the case of this passive sensor, this is not a problem as long as the power generated is sufficient to supply the electronics when there is a leak. Therefore, understanding the power output of the self-powered water leak sensor is essential. This includes understanding what conditions may cause the sensor to fail.

Integrating IoT and energy harvesting devices is clearly challenging because each energy harvesting technology is unique and has power output that is environment dependent. In the case of the self-powered sensor in this work, the environment can be extremely variable as water leak sensors may be useful in many conditions. Energy harvesting enables embedded developers to create more sustainable and compact designs, leading to increased attractiveness of products by extending battery life or eliminating the need for batteries altogether. This not only enhances the appeal of the product but also greatly reduces lifecycle costs. The growing concern among consumers and commercial organizations about e-waste, coupled with the introduction of new government regulations, has further raised awareness of our environmental challenges and the need for immediate action [28], [29], [44].

2.4 Redox Reactions and Metal-Air Electrochemistry

Electrochemical cells are devices that convert chemical energy into electrical energy through a redox (reduction-oxidation) reaction. Redox reactions involve the transfer of electrons between elements where one species undergoes oxidation (loses electrons), and another undergoes reduction (gains electrons). The driving force behind the redox reaction is the difference in the reactivity of the species involved. The anode material easily loses electrons, and the cathode material more easily accepts electrons [45], [46].

An electrochemical cell consists of two half-cells connected by a conductive pathway. Each half-cell is an electrode in an electrolyte solution. The electrode in the oxidation half-cell is the anode, while the electrode in the reduction half-cell is the cathode. The electrolyte solution contains ions that facilitate the movement of charge. During operation, the oxidation half-cell releases electrons, which travel through the external circuit to the reduction half-cell. This flow of electrons generates an electrical current. Meanwhile, in the oxidation half-cell, the anode undergoes oxidation, losing electrons and dissolving into the electrolyte as positive ions. In the reduction half-cell, the cathode attracts the electrons from the external circuit, causing a reduction reaction to occur. The reduced species gains electrons and may precipitate or form a compound [45], [46].

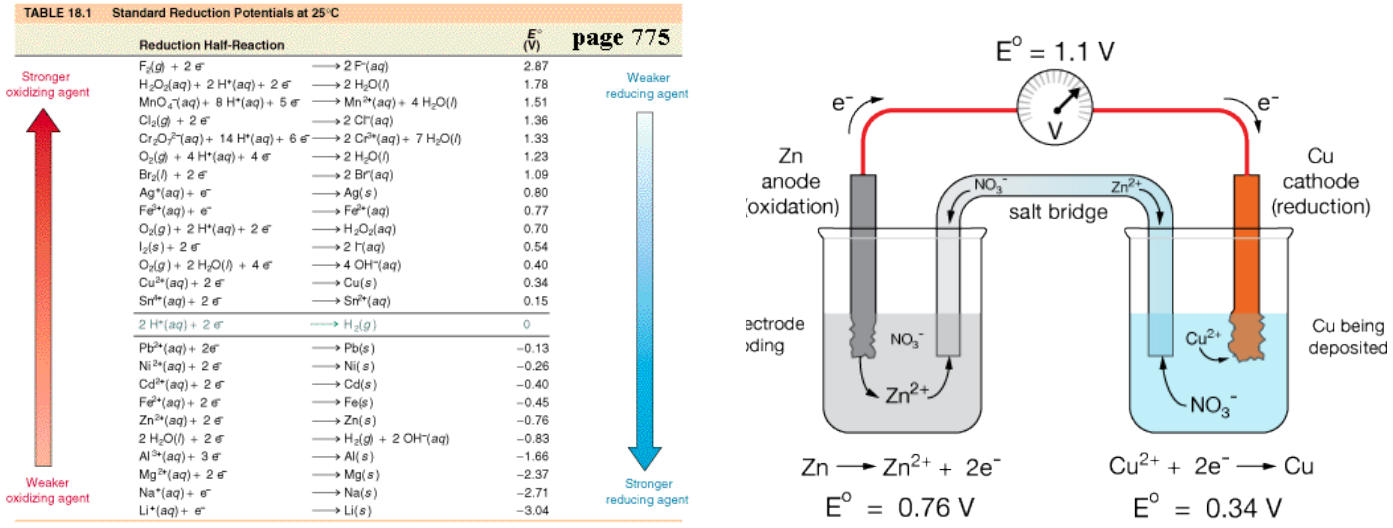


TABLE 18.1 Standard Reduction Potentials at 25°C

page 775

Reduction Half-Reaction	E° (V)
$F_2(g) + 2e^- \longrightarrow 2F^-(aq)$	2.87
$H_2O_2(aq) + 2H^+(aq) + 2e^- \longrightarrow 2H_2O(l)$	1.78
$MnO_4^-(aq) + 8H^+(aq) + 5e^- \longrightarrow Mn^{2+}(aq) + 4H_2O(l)$	1.51
$Cl_2(g) + 2e^- \longrightarrow 2Cl^-(aq)$	1.36
$Cr_2O_7^{2-}(aq) + 14H^+(aq) + 6e^- \longrightarrow 2Cr^{3+}(aq) + 7H_2O(l)$	1.33
$O_2(g) + 4H^+(aq) + 4e^- \longrightarrow 2H_2O(l)$	1.23
$Br_2(l) + 2e^- \longrightarrow 2Br^-(aq)$	1.09
$Ag^+(aq) + e^- \longrightarrow Ag(s)$	0.80
$Fe^{3+}(aq) + e^- \longrightarrow Fe^{2+}(aq)$	0.77
$O_2(g) + 2H^+(aq) + 2e^- \longrightarrow H_2O_2(aq)$	0.70
$I_2(s) + 2e^- \longrightarrow 2I^-(aq)$	0.54
$O_2(g) + 2H_2O(l) + 4e^- \longrightarrow 4OH^-(aq)$	0.40
$Cu^{2+}(aq) + 2e^- \longrightarrow Cu(s)$	0.34
$Sn^{4+}(aq) + 2e^- \longrightarrow Sn^{2+}(aq)$	0.15
$2H^+(aq) + 2e^- \longrightarrow H_2(g)$	0
$Pb^{2+}(aq) + 2e^- \longrightarrow Pb(s)$	−0.13
$Ni^{2+}(aq) + 2e^- \longrightarrow Ni(s)$	−0.26
$Cd^{2+}(aq) + 2e^- \longrightarrow Cd(s)$	−0.40
$Fe^{2+}(aq) + 2e^- \longrightarrow Fe(s)$	−0.45
$Zn^{2+}(aq) + 2e^- \longrightarrow Zn(s)$	−0.76
$2H_2O(l) + 2e^- \longrightarrow H_2(g) + 2OH^-(aq)$	−0.83
$Al^{3+}(aq) + 3e^- \longrightarrow Al(s)$	−1.66
$Mg^{2+}(aq) + 2e^- \longrightarrow Mg(s)$	−2.37
$Na^+(aq) + e^- \longrightarrow Na(s)$	−2.71
$Li^+(aq) + e^- \longrightarrow Li(s)$	−3.04

Stronger oxidizing agent

Weaker oxidizing agent

Weaker reducing agent

Stronger reducing agent

Fig. 5 a) Standard Reduction Potential Table [47], b) Zinc-copper electrochemical voltaic cell [48].

The determination of materials as anodic or cathodic is done using the standard reduction potentials (Fig 5a). The redox reaction requires two species, and the redox potential of a material pair is determined by the sum of the standard reduction potentials. For example, a common redox pair in batteries is zinc anode (0.76V) and copper cathode (0.34V) as seen in Fig. 5b. This cell would produce a voltage of 1.1V [45], [48].

Electrochemical cells find widespread applications. Electrochemical cells play a vital role in batteries and corrosion processes. Batteries are the most well-known example, where chemical reactions within the cell produce electrical energy [49], [50] [51]. They power numerous portable devices, vehicles, and even large-scale energy storage systems. Fuel cells, a type of electrochemical cell, generate electricity by continuously supplying reactants, such as hydrogen and oxygen [52], [53], [54]. They are employed in stationary power generation, transportation, and other areas. When metal is exposed to an electrolyte, it can undergo oxidation, leading to its corrosion. Understanding these redox reactions aids in developing strategies to prevent and mitigate corrosion.

2.4.1 Metal-Air Cells

Metal-air electrochemistry refers to the study of electrochemical reactions involving metal electrodes and oxygen from the surrounding air. These systems typically involve a metal electrode as the anode and oxygen as the cathode [55]. The metal can be various types, such as zinc, iron, aluminum, or lithium, while the cathode is typically atmospheric oxygen [52], [53], [56]. The metal in this case is specifically a metallic solid, not a metal ion which vastly increases the theoretical energy density due to the density of metals as seen in Fig. 6. In a metal-air cell, the metal at the anode undergoes oxidation, releasing electrons and metal ions into the electrolyte solution. At the cathode, oxygen from the air is reduced, accepting electrons, and forming oxide or hydroxide ions. The overall cell reaction in metal-air electrochemistry involves the combination of the anodic and cathodic reactions [57].

$$M \rightleftharpoons M^{n+} + ne^-$$

$$O_2 + ne^- + 2H_2O \rightleftharpoons 4OH^-$$

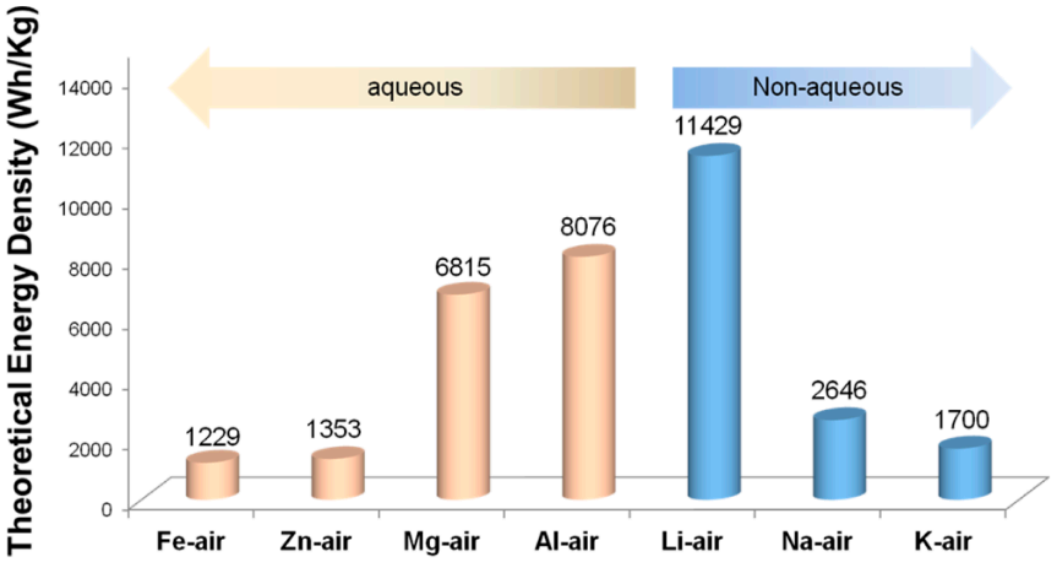


Fig. 6 Theoretical Energy Densities for Different Metal-Air Batteries [58]

Metal-air cells may have an aqueous or non-aqueous electrolyte, however in this work the focus will be aqueous electrolyte since the focus is water-based power generation. Common metals used in aqueous metal-air batteries are reactive in water such as Zn, Fe, Al, and Mg. These materials tend to corrode or oxidize in water producing either metal oxides or hydroxides. The downside of these materials is that the oxidation reaction is not always easily reversible, meaning that batteries using this system would not typically be rechargeable. While metal-air batteries can have a variety of morphologies, common structures of metal air batteries can be seen in literature in Park 2015, and Li 2017 and are exhibited in Fig. 7 [58], [59].

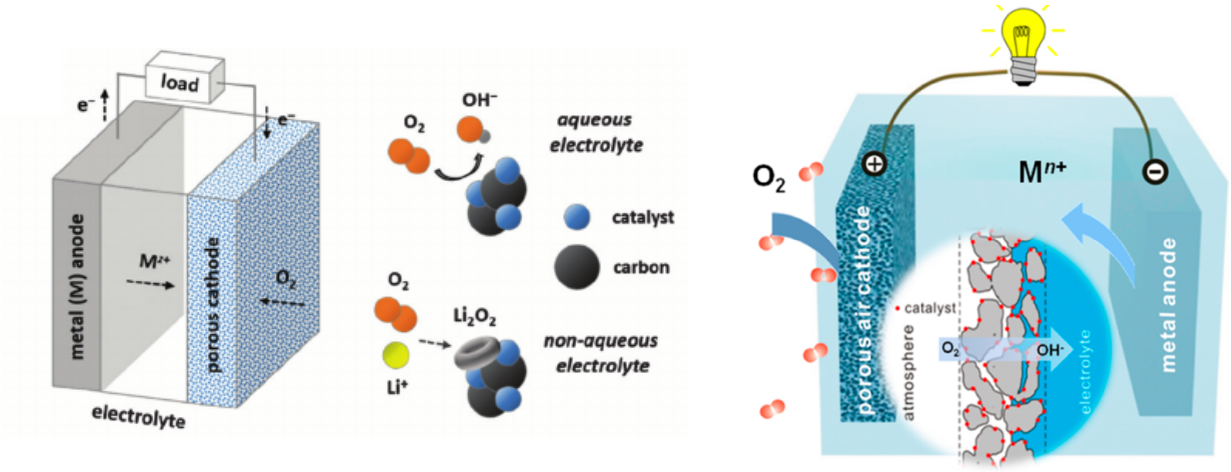


Fig. 7 a) Schematic of metal-air battery from Park 2015[59], b) Schematic configuration and operation principle for aqueous metal−air batteries from Li 2017. The oxygen reduction reaction taking place at the porous air cathode is displayed in the inset. [58]

Metal-air batteries offer several advantages, including high energy density, lightweight design, and the ability to tap into the abundant source of atmospheric oxygen [60]. They have potential applications in portable electronics, electric vehicles, and grid storage [61]. Zinc-air batteries are used in hearing aids, due to their long-lasting and low-cost characteristics. However, metal-air systems also face challenges. One major issue is the limited shelf life and rechargeability of these batteries. The presence of moisture and carbon dioxide in the air can lead to the gradual degradation of the electrolyte and affect the performance of the cell. Additionally, the formation of unwanted side reactions, such as the generation of hydrogen gas in zinc-air batteries, can reduce efficiency and pose safety concerns [62].

Research is ongoing to address these challenges and improve the performance and longevity of metal-air batteries. However, in the case of designing a self-powered sensor, the issues of are not as relevant as long as a threshold of repeatability can be reached. The main design of this sensor is very close to a metal-air cell in aqueous electrolyte, with graphite acting as a scaffold for the oxygen reduction reaction.

2.5 Aqueous Magnesium Electrochemical Cells

The water induced chemical reaction system is utilized to make a self-powered water leak detection device. The magnesium metal is used to carry out this work since it undergoes oxidation reaction when reacts with water [63]. Magnesium is a reactive, alkaline earth metal that is abundant in earth's crust [64]. This water leak detection device uses AZ-31 alloy of Mg which have various elements with different approximate minimum and maximum ratios as mentioned in Table 3 [65].

Table 3: Composition of AZ31b by Weight

Element	**Amount in AZ31b (wt.%)**
Magnesium	97
Aluminum	3.5
Zinc	1.4
Manganese	0.2
Silicon	0.3

Magnesium has been used to create primary batteries. It is well known that Mg metal reacts readily with air and water in an oxidation reaction, where a passivating layer is formed [66]. And since Mg has two valence electrons, it loses those electrons and forms a Mg2+ ion or a stable compound upon reaction with oxygen and hydrogen present in water. The reactions between Mg and water are presented below [67]:

$$Mg(s) \rightarrow Mg^{2+} + 2e^{-}$$

$$H_2O \rightleftharpoons H^{+} + OH^{-}$$

$$Mg(s) + 2H_2O\ (l) \rightarrow Mg(OH)_2 + H_2(g)$$

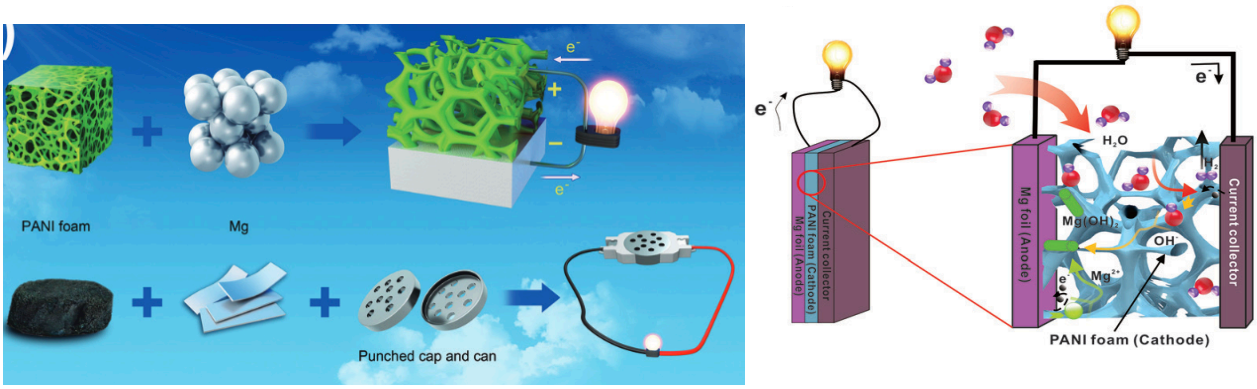


Fig. 8 a) Magnesium water coin cell [68], Polyaniline foam scaffold for cathodic reduction in aqueous magnesium battery [69]

This overall redox produces a redox potential of 2.37 V in standard conditions. This reaction has been used in multiple primary batteries because it is very difficult to reverse. Two significant examples of these aqueous magnesium cells are demonstrated in Hongyang 2009 and Xie 2015 (Fig. 8) [68], [69]. Xie uses this system in a coin cell for small scale applications while Hongyang is designed to be a sea water reserve battery. Aqueous magnesium batteries are a promising energy storage technology that utilizes magnesium ions in an aqueous electrolyte solution. They offer several advantages over traditional lithium-ion batteries, such as higher energy density, lower cost, and improved safety due to the non-flammability of the aqueous electrolyte. However, challenges remain, including limited cycling stability and slower reaction kinetics [65], [66]. These are not necessarily problems in the design of a self-powered sensor.

2.6 Graphite Oxidation and Power Generation Applications

Graphite is commonly used as an electrode material in various electrochemical systems, including batteries and fuel cells. Graphite possesses several properties that make it suitable for electrode applications. It is an excellent conductor due to its abundance of sp2 carbon. Its layered structure consists of hexagonally arranged carbon atoms bonded together in a two-dimensional plane [70-74]. This arrangement allows for easy movement of electrons within the graphite structure, facilitating efficient electron transfer during the reduction reactions (Fig. 9). Graphite also has a high surface area and many sites for the oxygen reduction reaction to occur. The layered structure of graphite provides numerous exposed surfaces where electrochemical reactions can take place [71], [72]. Additionally, graphite exhibits chemical stability. It is resistant to chemical reactions, corrosion, and degradation under normal operating conditions. This stability is crucial for the long-term performance and durability of the cathode material [73]. Graphite is not known in literature to oxidize in air at room temperature and only oxidizes in atmosphere at temperatures above 400°C. When graphite is oxidized, the structure changes slightly. Oxidation on the edges of the structure

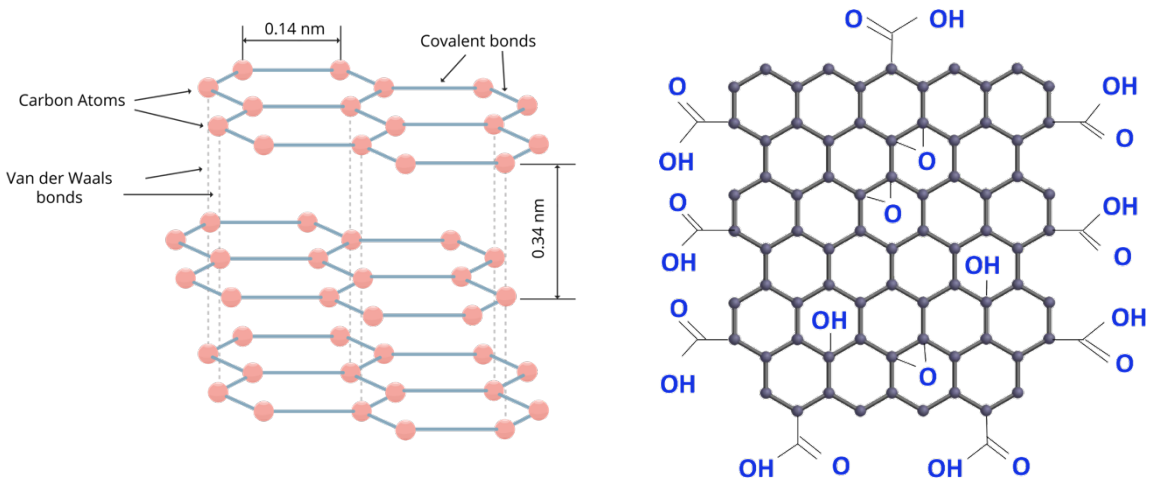


Fig. 9 a) Flake graphite has a layered structure constituting carbon atoms in a hexagonal lattice [73], b) The graphene oxide molecular structure consists of carbon, hydrogen and oxygen [74].

result in dangling oxide and hydrogen bonds. Oxidation within the graphite structure breaks the sp2 planar network and can change the conductivity of graphite [71], [73], [74].

When used as a cathode, graphite serves as the site for reduction reactions, where it accepts electrons and participates in the electrochemical reactions. There are a few applications in literature with graphite cathodes. In battery applications, graphite is commonly used as the cathode material in lithium-ion batteries as an intercalation medium [75], [76], [77]. Jiang 2017 describes a graphite-manganese oxide composite used as a fuel cell cathode [78]. It should be noted that graphite is often not directly involved in electrochemical reactions especially at the cathode [77], [78], [79]. It is used as a scaffold or catalyst and the location of the reduction reaction by adsorbing electrochemically active species.

2.7 Self-powered Water Leak Detector Prototype

A self-powered water leak detector was designed and fabricated based on the magnesium-air battery [19], [20], [64]. As mentioned in Chapter 1, this sensor has a materials stack (Fig. 2) with well-matched materials. The sensor in this work uses a materials stack of magnesium and graphite and uses a reaction with water to power the sensor and send a notification to the end user. The essential function of the self-powered mechanism in the sensor is described below in Fig. 10 in a similar sensor that uses CNF rather than graphite. Graphite was chosen as a more cost effective option with no decline in sensor performance.

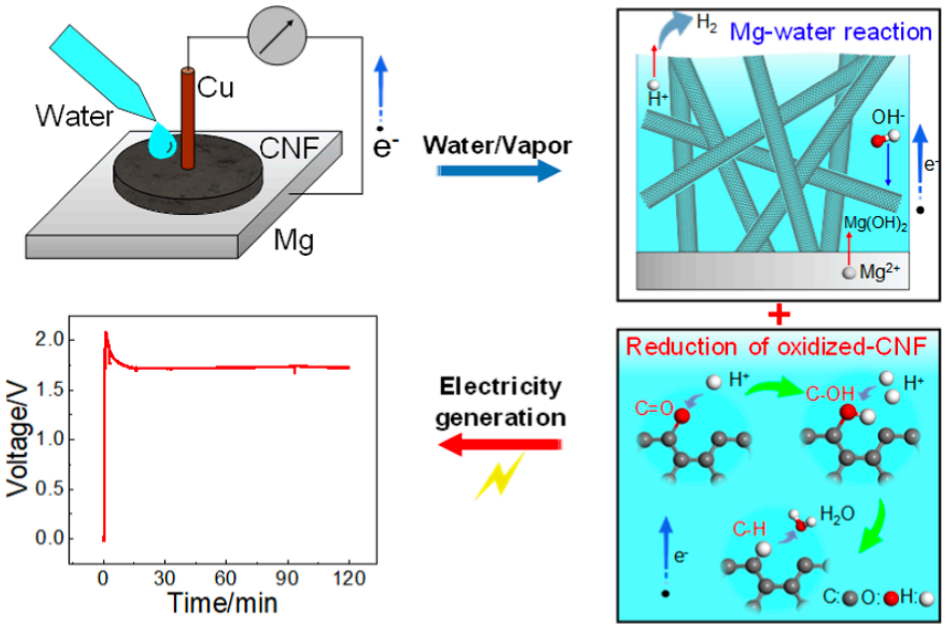


Fig. 10 Schematic of the Mg−CNF device used for water detection, as well as the Mg−water reactions and ion transportation happening in the CNF porous structure [63].

2.8 Summary

This chapter first established the problem of water leaks and their growing effect on society. Then water leak detectors were introduced along with their major issues – battery life, and limited sensor placement. Next IoT devices were explored and the motivation for integrating energy harvesting technologies with IoT was explained. The specific use of metal-air batteries was described as it relates to the magnesium-graphite based power source investigated in this work. Next, the electrochemical interactions of magnesium and graphite were explored in order to give context for the self-powered water leak sensor design. Finally, the self-powered water leak sensor prototype was described along with its function.

Chapter 3
Experimental Methodology and Characterization Methods

3.1 Sample Preparation and Sensor Components

As the sensor is not powered by any battery, it needed to be able to harvest its own power. This is how the research team came out with the idea to power thanks to the reduction potential difference between the oxidation of magnesium and water.

The leak sensor is design with two parts to combine: a sensor unit and an electronic unit (Fig 11). The sensor unit is built with (from the bottom to the top of the unit):

1. Filter paper that connects to the outside of the sensor
2. Pressed graphite palette
3. A second filter paper (same shape as the piece of graphite)
4. Magnesium sheet (metal anode)

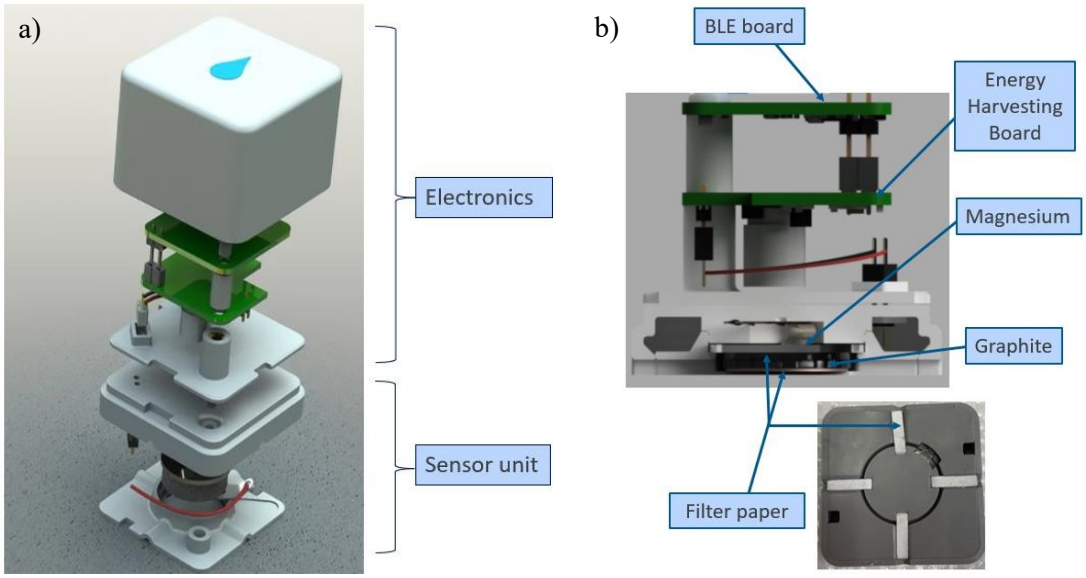


Fig. 11 a) Blown up render of the self-powered water leak detector in this work including both the sensor unit and electronics [18] b) Components of leak detector [18]

3.1.1 Sensor Materials

Graphite is a major component of the sensing materials. Powdered graphite is used as opposed to solid graphite so water can flow through the piece. These graphite powder pieces were delicate and prepared manually. Synthetic powdered graphite from Aldrich-Sigma with average particle size 20μm was used. The graphite is pressed using a mold (Fig 12b) that fits 300mg which is then pressed in an Instron Tensile Tester to 100N (Fig12a).

Magnesium pieces are essential to sensor function. The AZ31b alloy was used. Magnesium sheet is punched into coins with 1.5cm diameter. The sheet has a protective died layer that must be removed. Both surfaces were sanded until they were smooth and shiny using 400 grit sandpaper with water and lubricant (Fig 1d). Next, the filter papers are prepared. These are qualitative filter paper from Cytiva that are laser cut into two shapes as seen in Fig 12e.

3.1.2 Assembling sensor unit

After materials preparation, the sensor was assembled. In the materials only tests, the materials were simply stacked. The in-package samples were encased in an ABS packaging (Fig 12c). First a later of filter paper was placed, then graphite, another filter paper and magnesium. There are two distinct probes: one on the bottom connecting to the graphite, and the second one to the magnesium.

From here the device connects to the electronics: an energy harvesting board and a Bluetooth Low Energy (BLE) chip. The sensor function is as follows: First, the filter paper goes out of the packaging to improve the detection of small leaks. Then, the water is absorbed inside the sensor via the filter paper and goes through the graphite pieces thanks to porous channels. Afterwards, a second filter paper in direct contact with magnesium absorbs the water. The oxidation reaction between magnesium and water happens at this interface. The reaction generates power and allows the activation of the BLE chipset that will communicate with the

gateway and send the data to the cloud. The data is processed and sent the user via email. In standard conditions, the sensor can send a notification in less than a minute.

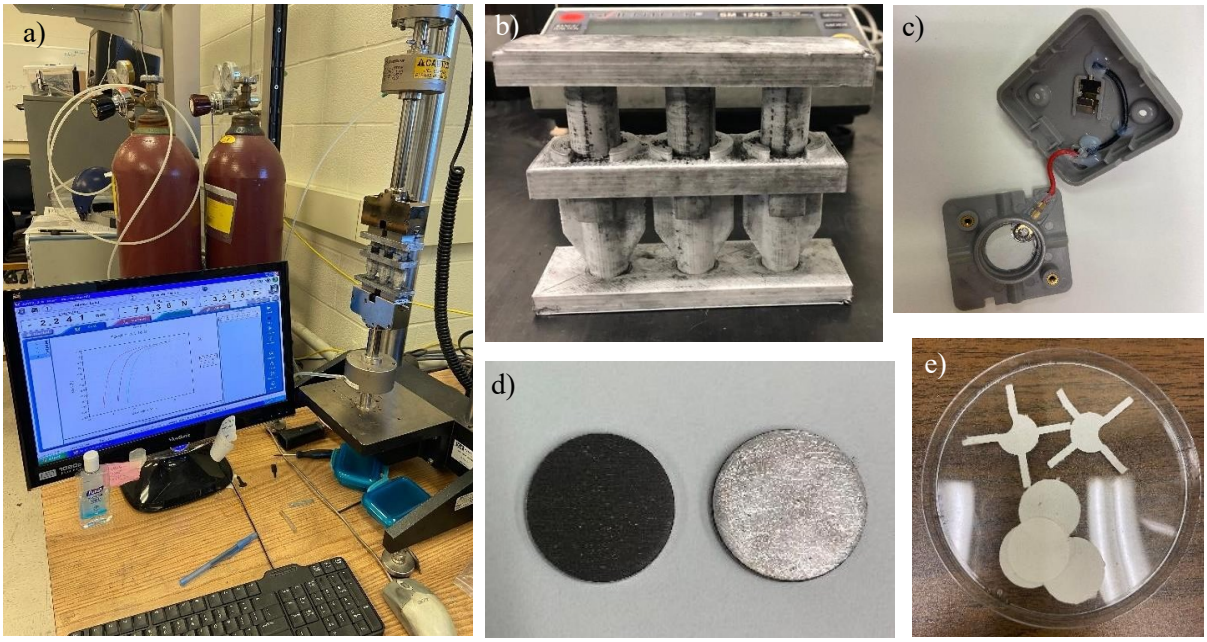


Fig. 12 a) Instron tensile tester used for pressing graphite, b) graphite press mold, c) open sensor package without materials, d) magnesium sheet before and after sanding, e) filter paper pieces

3.2 Characterization Methods

3.2.1 SEM and EDX

Scanning electron microscopy (SEM) is a characterization tool that can be used to provide images of micro and nano structures under high magnification, with high resolution and depth of field. The working principle of the SEM is the interaction between high energy electrons and the material of the sample. A focused electron beam is incident on the sample and scans over a region of the sample. Electrons are then scattered or ejected and detected. The signals from the detector are accumulated and processed to produce the SEM micrograph [80]. SEM is extremely useful due to its ability to resolve surface details on the micro and nano scale. Image resolution is the limit of how close two points on a sample can

be before they are no longer distinguishable as separate. Image resolution is wavelength dependent as shown in the equation below.

$$d = \frac{\lambda}{2nsin\theta} = \frac{\lambda}{2NA}$$

Additionally, the resolution of SEM images depends on the wavelength of high energy electrons between two points that can be. The wavelength of electrons used for SEM are on the order of 0.1 to 0.01nm, enabling high resolution of very fine details on the nano scale [80], [81].

3.2.2 XPS

The XPS system in WatLab uses an aluminum X-ray source as well as a monochromator which can decrease background peaks due to bremsstrahlung and reduce peak broadening.

The general procedure when running XPS is to first take a low-resolution survey scan from 0eV to 1200eV. The initial step size for is 0.5 eV with a pass energy of 50eV. This detects the elements present quickly. Next, the major peaks re identified and a higher resolution scan around the relevant binding energies will take place. For this high-resolution scan, the step size is 0.1eV and the pass energy is 30eV. If the signal to noise ratio is poor, which is expected for smaller peaks, multiple scans can be used to decrease the background noise. The high-resolution peaks deconvoluted to elucidate the bonding behaviour and differences between the samples. Since the sample material is graphite, which is relatively stable, there is no concern about the sample being damaged by X-rays.

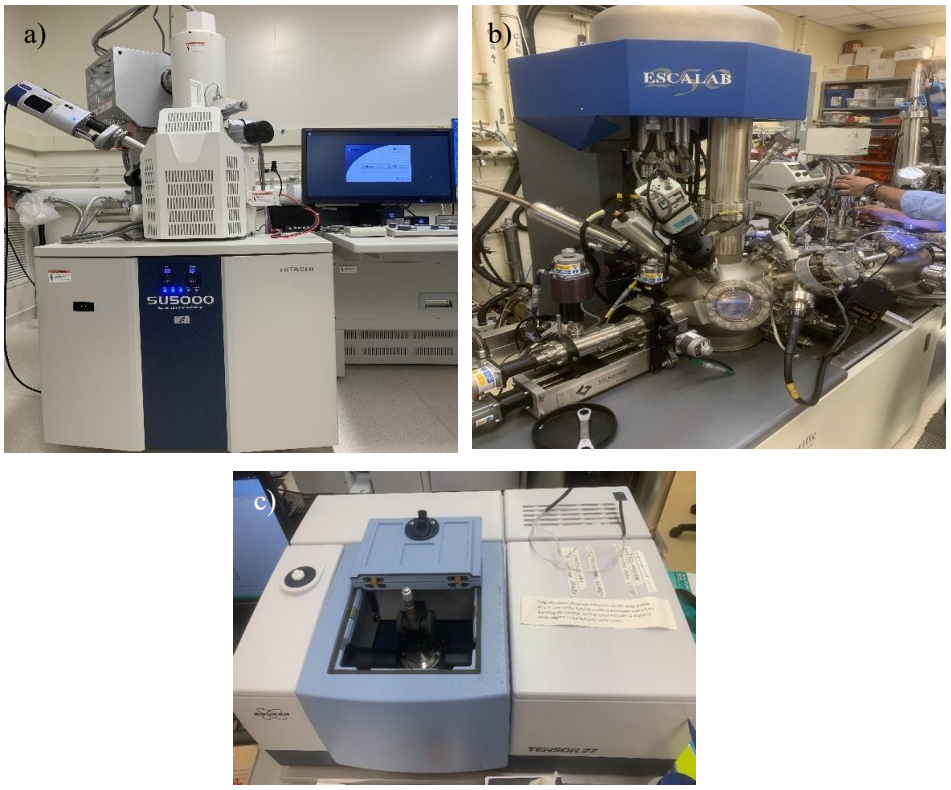


Fig. 13 a) SEM and EDX Instrument; b) XPS Instrument; (c) Raman

3.2.3 Raman

Raman spectroscopy is another type of vibrational spectroscopy and is based on Raman scattering. Light that is incident upon Raman active materials scatters both elastically and inelastically. Inelastically scattered light has a different frequency from incident light and is called Raman scattering. Scattered photons with lowered frequency have undergone Stokes scattering whereas scattered photons with increased frequency have undergone anti-Stokes scattering. Since Stokes scattering is generally higher intensity than anti-Stokes scattering, Stokes scattering is used more commonly for spectroscopy. The changes in light frequency are the Raman shifts which are plotted to create the Raman spectrum of a material [82],[83].

Raman spectroscopy and FTIR spectroscopy are often used as complementary methods for material identification [80].

3.3 Test Set-up for Electrical Measurements

3.3.1 Experimental methodology

The primary method of evaluating the electrical performance is the load test [9]. This test involves placing a voltmeter across the sensor to read the voltage output for 4 to 5 minutes. As the voltage is being read, a load of 50μA is applied. This results in a voltage drop when the current is applied, however this is typically small (<1V). There are two configurations for this test:

1) Materials-only: This kind of test enables to check the performance without any side effects from the packaging or the circuit. The sensing materials are stacked from bottom to top in the following order: magnesium, filter paper and graphite on top. The voltage was measured by a probe inserted into the graphite top and another lead connecting to the magnesium. Another parallel circuit is used to apply the load Then, to run those tests, a multimeter is connected, and data is collected into the Keysight Benchvue software. This test is typically done at standard conditions and uses 500μL of water dropped directly onto the top surface of the graphite.

2) In package: In this test, the sensor packaging without electronics is tested with the DMM and same current load. In this case, the full sensor unit is placed into a Petri plate a with 0.5cm depth of water to test the sensor to ensure it is in an excess of water. The measurement with the DMM starts when the sensor is placed inside water while the load from source meter is turned ON once the sensor reaches its maximum voltage around 2.0 V.

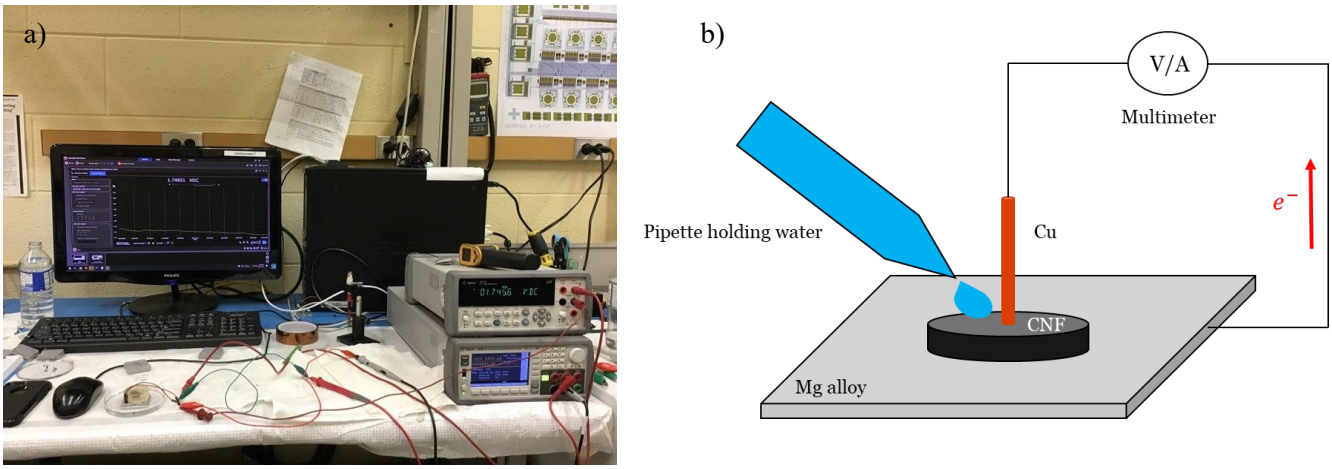


Fig. 14 a) Experimental set-up for the in-package test without electronic unit, b) schematic of materials only test setup

3.3.2 Sensor Behaviour at Standard Conditions

To plot the results obtained, a python script was developed using matplotlib and seaborn modules This code aims to align all the maximum voltages so we can easily observe and compare the shape and the evolution of the curve from the different samples or experiments. Moreover, it highlights the time needed to reach the maximum voltage and thus to activate the sensor. An example of this plot can be seen below in Fig. 15. This plot displays the standard behaviour as a result of the load test mentioned above with n=8. These samples were tested at 25°C, 27% relative humidity and standard pressure The ideal behaviour is an average voltage around 2.0V with a minimal drop in voltage as the load is applied. As seen in the inset image in Fig. 15, there is no sharp drop when the load is applied. These results will serve as a standard to compare load test results to in varying environmental conditions.

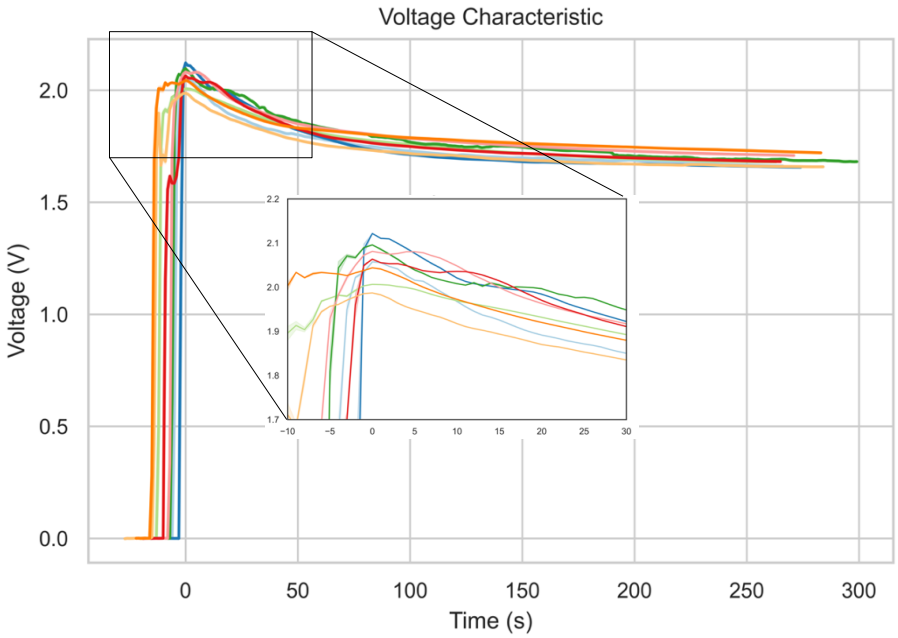


Fig. 15 Standard load test results at 25°C, n=8. Inset shows higher resolution of peak

3.4 Summary

This chapter describes the manual sample preparation of both the materials stack and the sensor materials in the packaging. It also fundamental methods of characterizing the graphite including SEM, XPS, and Raman as well as the limitations of these methods. Additionally, it establishes the load test method of electrical testing for both the materials stack and the packaged sensor. Finally, it includes a description of the expected behaviour of the sensor in the load test that can be used in comparison with other load test data as conditions are changed.

Chapter 4
Role of Graphite in the Sensor

4.1 Introduction

The main goal of this chapter is to gauge role of graphite in the sensor. The sensor is primarily driven by a redox reaction between magnesium and water. The graphite piece is considered an absorbent material that brings water to the surface of magnesium and is the location for the oxygen reduction reaction. However, some observed changes in the graphite indicate that the palette changes as it is used.

In order to understand the role of graphite in the overall reaction in the sensor the interactions between graphite and sensor usage were studied. The likely mechanisms of interaction are well known processes such as corrosion and oxidation of the materials involved over time. It is essential to determine the negative impact of these processes on the function of the sensors. In this chapter, the effect of sensor usage on graphite palette is characterized using SEM, Raman, and XPS and combined with a real-time shelf-life test to provide a complete picture of the role of graphite in the sensor.

4.2 Sample Conditions

The characterization in this section is done after the graphite palette has been exposed to different conditions indicated with the following codes: DG, GS, MS, MS5.

DG samples are very similar to the graphite in the state that it was ordered, the only difference being the pressing process. GS samples are pressed and exposed to water, however they are on the inert glass surface, so the only interaction is between graphite and water. In literature, there is no interaction between graphite and water at standard conditions. MS samples are pressed and placed on magnesium with 50μA applied load. Water is applied to these samples and the redox reaction between magnesium and water is expected to occur

across the graphite. This condition also includes a voltmeter placed across the magnesium and graphite as shown in Chapter 3. This is the load test condition, which is close to the conditions that occur inside the sensor. The MS5 samples go through the same conditions of the MS samples 5 times, with a 2-day drying period in between each cycle. All samples are dried before testing with any characterization method.

4.3 Graphite Hydrophobicity

The oxidation reactions of graphite in water and air are well known. Graphite oxidizes in oxygen-containing atmosphere into CO_2 at temperatures above 400°C.

As described in Chapter 3, the first observations of the materials stack were done outside of packaging. In this materials system, there is an observed difference in behaviour between newly pressed graphite pieces and graphite pieces that have gone through one cycle of being wet and then have dried off. The sensor materials being wet, drying and being re-wet is a fundamental process of the sensors which, as explained in Chapter 3, go through multiple uses. In this experiment the volume of water used is 500µL. The observed behaviour is that

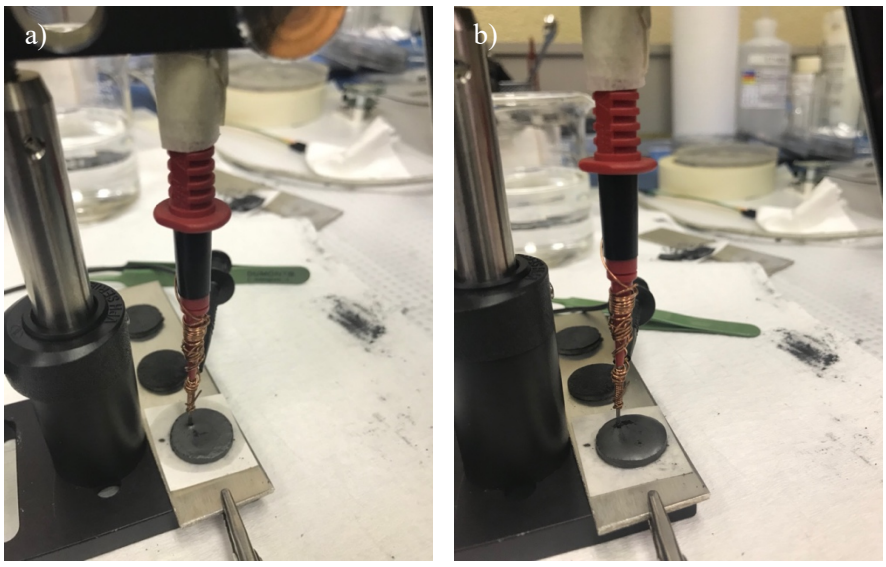


Fig. 16 a) Hydrophilic nature of graphite palette and b) after one drying cycle, graphite is noticeably hydrophobic.

newly pressed graphite pieces absorb water quickly. Water penetrates the graphite to reach the magnesium surface readily. However, graphite pieces that have gone through at least one cycle of drying and being re-wet absorb water more slowly, and have water sit on the surface, suggesting a more hydrophobic graphite pallet (Fig. 16). Interestingly, this difference is also seen in dry graphite pieces that are kept uncovered for at least 1 week. This might indicate that aging due to repeatability and atmospheric conditions have similar mechanisms.

Two mechanisms may be hypothesized here:

a. The difference in behaviour is caused because of a change in oxidation of the graphite. In literature, there is a difference in hydrophobicity of graphene and graphene oxide which suggests the oxide content of the graphite changing. This may be due to a reaction with the atmosphere, or water.

b. The graphite is changed by the reaction with magnesium. As mentioned in Chapter 2, the magnesium does not produce or consume oxygen in the corrosion reaction with water. However, magnesium can consume oxygen in a separate reaction to produce magnesium oxide. Additionally, magnesium ions may infuse into the graphite dissolved in water, which may change the hydrophobicity of the graphite piece. It must be noted that the change in hydrophobicity is observed on the top surface of the graphite that is not is contact with the reactive surface, this may indicate that this shift is not a result.

4.4 SEM Particle Analysis on Graphite

Scanning electron microscopy was used to investigate the morphology of the graphite pieces. The graphite was imaged at 5000x magnification at 5.00 kV in Fig 17. Since the graphite powder is made entirely low mass elements (carbon and oxygen) it was not analyzed using the BSE detector because there would be very little elemental contrast. The SE2 image (Fig. 17 a) is very dark. It still has higher contrast between the highest and lowest features than the InLens image. The InLens image is very bright and is higher resolution than the SE2 image around the edges of the graphite particles. The 5000x image shows individual graphite particles and shows that the morphology of graphite particles is very flaky and flat, analogous to a 2-dimensional material.

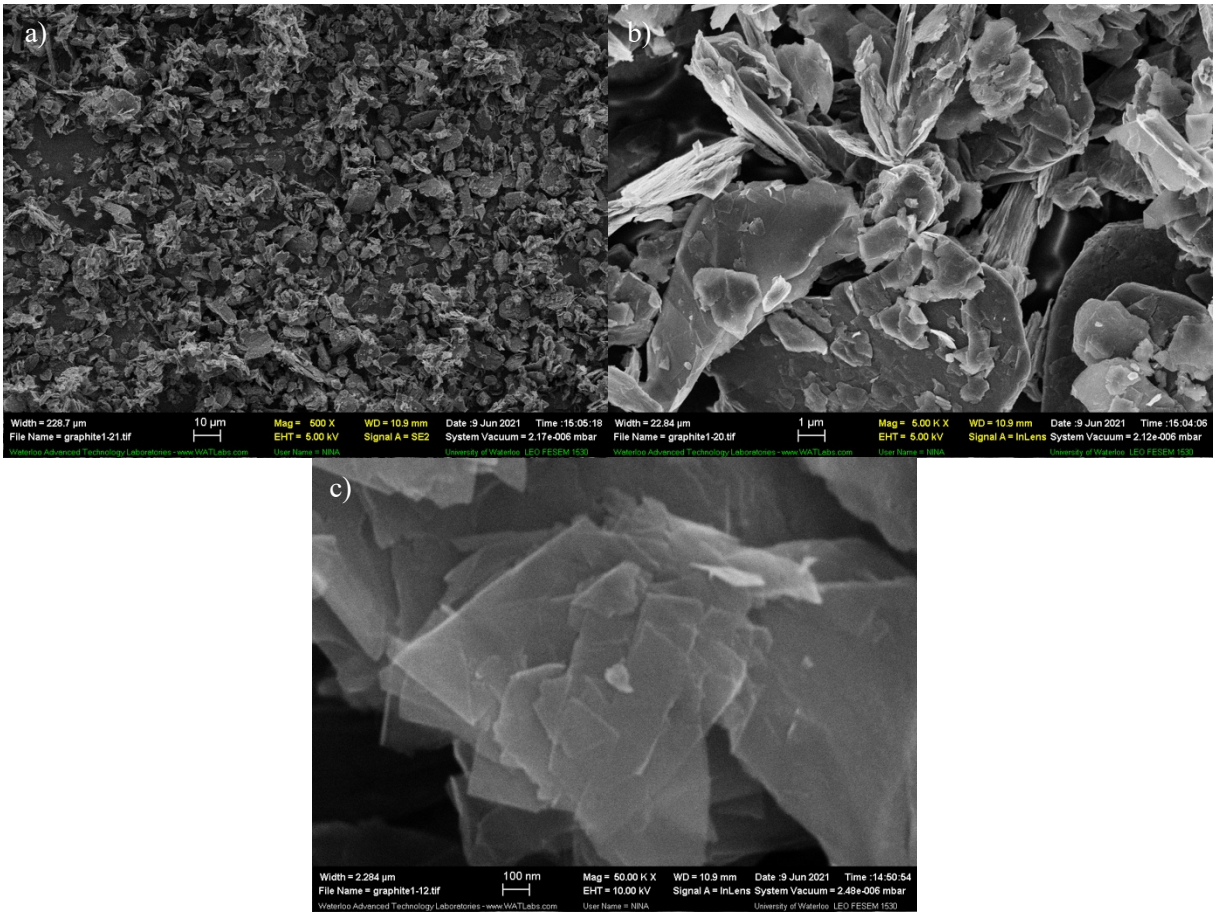


Fig. 17: Image of graphite particles at a) 500x magnification using SE1: b) 5.00kV, c) 20.00kV

Layered graphite flakes at 5000x magnification, and 20.00kV were scanned in Fig 17c. Fig. 17 shows a) an SE2 image and b) an InLens image. The resolution of the SE2 image is poor when compared to the InLens image. The InLens image shows more details around the edges of each flake of graphite. The SE2 image still does show individual pieces of graphite but it appears blurry and unfocussed at high magnification. The graphite was imaged at 5000x magnification at 5.00 kV in Fig. 17b. Since the graphite powder is made entirely low mass elements (carbon and oxygen) it was not analyzed using the BSE detector because there would be very little elemental contrast. The InLens image is very bright and is higher resolution than the SE2 image around the edges of the graphite particles. The 5000x image shows individual graphite particles and shows that the morphology of graphite particles is very flaky and flat, analogous to a 2-dimensional material.

4.5 EDX Elemental Analysis on Graphite

EDX was used to analyze the elemental composition of the graphite samples. These samples were separated into 4 categories with n=6:

a. Dry pressed graphite (DG)
b. Graphite that has been exposed to water on a glass slide (GS)
c. Graphite that has been exposed to water on a magnesium sheet (MS)
d. Graphite that has been exposed to water on a magnesium sheet for 5 cycles (MS5).

Two of these EDX spectra are shown in Fig. 18. The samples displayed represent the two extreme sample conditions. Fig. 18a, c display the DG condition and Fig. 18b,d display the MS5 condition. EDX is a process paired with SEM imaging and so the relevant SEM images are also included. In Fig. 18a, b the SEM imaging shows that at 1000x magnification, there are no visible differences between these two samples, as also determined in chapter 4.2. The samples only displayed two elements prominently, carbon and oxygen. This is consistent

with the testing method; however, it is interesting that no elemental magnesium was detected. The major change in EDX spectra is in the oxygen content, which is reflected in a lower

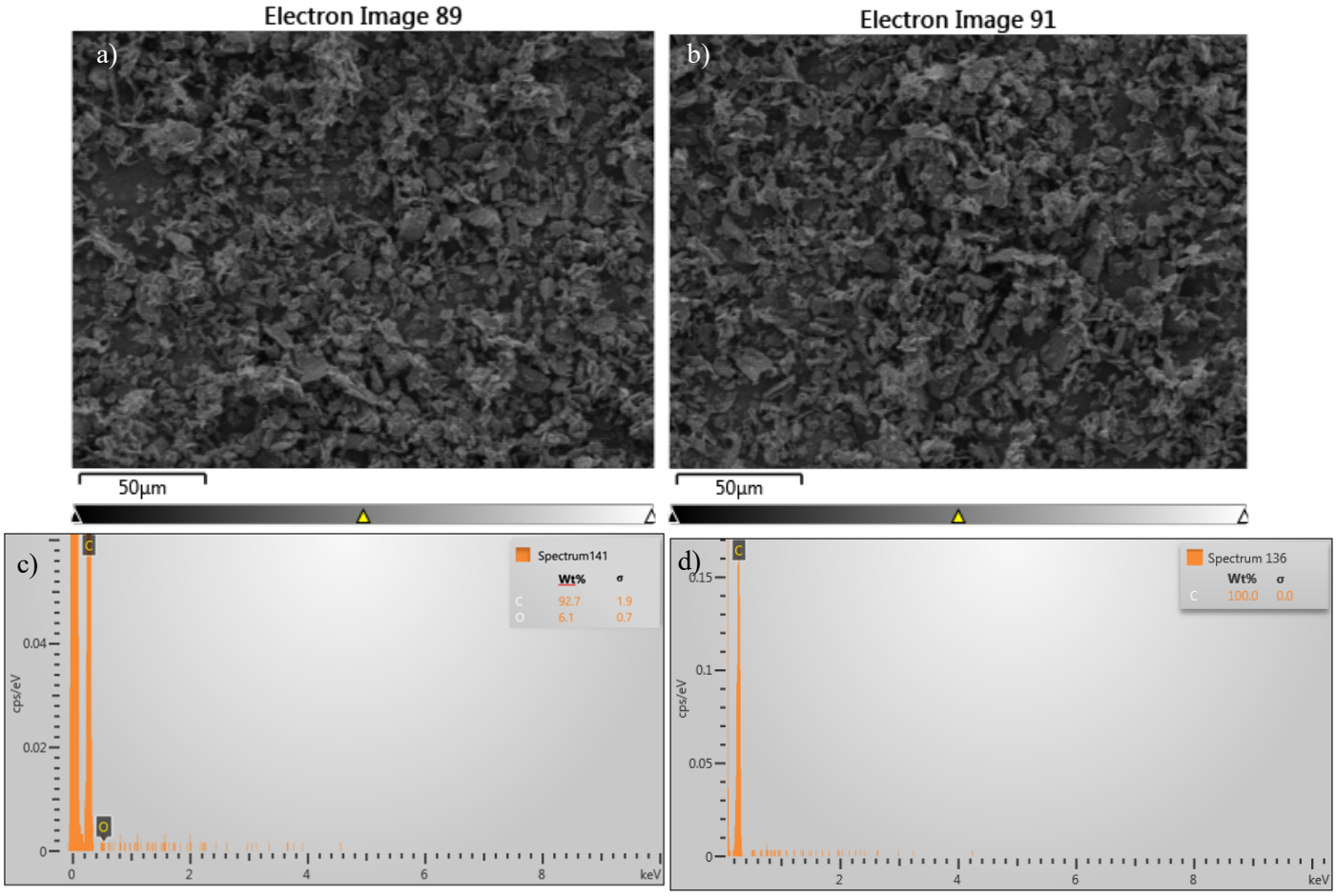


Fig. 18: EDX for graphite. a) SEM image of graphite for Spectrum 141, b) SEM image of graphite for Spectrum 141, c) EDX of graphite for Spectrum 136, d) EDX of graphite for Spectrum 136

carbon content as well, since the elevated presence of one element means that another appears less for a given region. The oxygen content for these EDX samples is summarized in Table 4.

Table 4: Oxygen and Carbon Content in Graphite Samples Under 4 Conditions

Sample	Sample Condition	Oxygen Content (wt%)	Carbon Content (wt%)
1	DG	5.9	93.8
2	DG	5.6	93.8
3	DG	5.5	93.5
4	DG	6.1	92.7
5	DG	5.8	93.8
6	DG	5.5	93.9
7	GS	4.3	94.7
8	GS	4.4	95.4
9	GS	4.3	95.1
10	GS	5.4	94.2
11	GS	5.0	94.7
12	GS	5.3	93.7
13	MS	3.1	96.2
14	MS	4.0	94.8
15	MS	3.3	96.6
16	MS	3.9	95.7
17	MS	3.6	96
18	MS	3.4	96.1
19	MS5	1.0	98.8
20	MS5	2.3	97.6
21	MS5	0.9	98.9
22	MS5	0.3	99.6
23	MS5	2.2	96.8
24	MS5	1.6	97.7

In each spectrum, the elemental composition of graphite with respect to carbon and oxygen were analyzed primarily as these were the only elements that appeared on the spectra. In Fig. 18c, which is a DG sample, the elemental composition was found to be 92.7wt% carbon and 6.1wt% oxygen. The average DG graphite sample was found to have. Graphite is expected to be a pure allotrope of carbon, and so it is determined here that the initial state of graphite as ordered is slightly oxidized.

The oxygen presence is not high enough to classify the graphite as reduced graphite oxide however, which typically has a maximum oxygen content of 20wt% [84]. In Fig. 18d, which is the MS5 condition, the elemental composition is 100wt% carbon and 0wt% oxygen. The average elemental composition of oxygen is as follows: DG: 5.1, GS: 4.8, MS: 3.1, MS5:1.4.

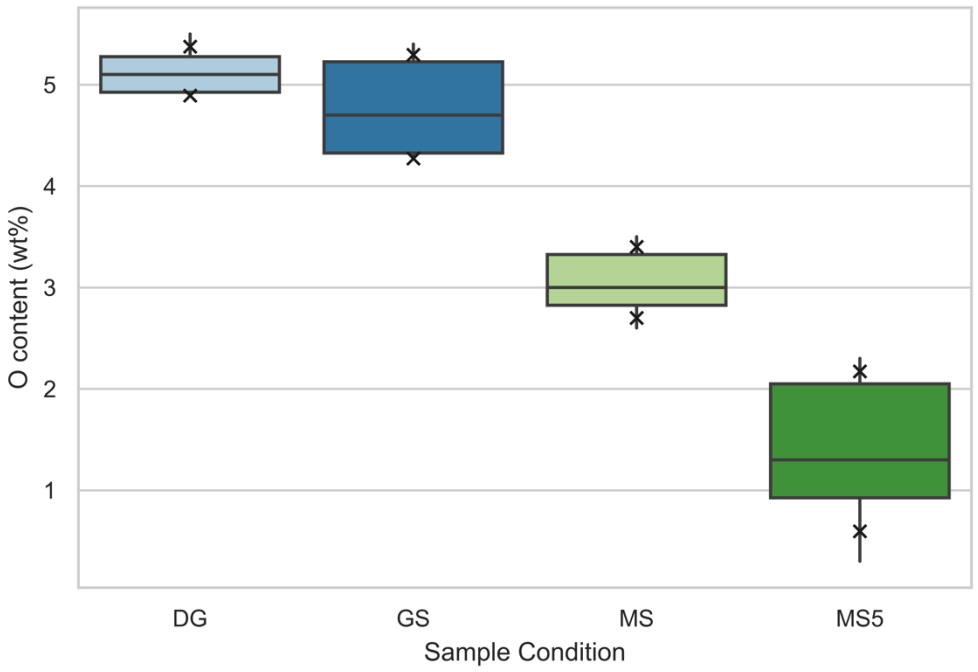


Fig. 19: Boxplots of the EDX oxygen content across 4 conditions. The measure of central tendency is the mean. Standard deviations are plotted as 'x'

In order to determine that these results were significant and not a result of random averaging bias, they were plotted on a box and whisker plot shown in Fig. 19. This plot shows that there is overlap between the ranges of the DG and GS samples, however, the effect of the MS and MS5 samples seem significantly different with no overlap in range or standard deviation.

The EDX analysis found no evidence of magnesium ions deposited in the graphite even in the. graphite used many times. The graphite is protected by a filter paper sheet and magnesium hydroxide has very low solubility in water. These results may indicate that exposure to MS or MS5 conditions affect adsorbed oxygen and may result in a slightly reduction effect on surface graphite. Graphite is known as the location of the reduction reaction in the overall power generation reaction of the sensor; however, it may also be involved in the reaction.

It is important to note that in EDX analysis, lighter elements have a high level of quantification error (around 2-5%) due to the bremsstrahlung effect, where characteristic lines for light elements are obscured by continuous spectrum caused by electron deceleration. In other words, when a charged particle, such as an electron, moves through a material, it can lose energy by colliding with the atoms or nuclei in the material. This loss of energy results in the emission of Bremsstrahlung radiation, which has a continuous spectrum of wavelengths and is often observed in X-ray and gamma-ray sources. For light elements, bremsstrahlung can obscure a significant portion of characteristic peaks [82]. Since the elements analyzed were carbon and oxygen which are much lighter elements, further analysis with other analysis tools can be used to add evidence of an observed pattern.

In conclusion, however, it was found using an experiment with 24 samples that oxygen content in graphite seemed to reduce when the graphite pallet was exposed to water and then dried before testing. Additionally, it was found that this effect was amplified when involved with in the redox reaction with magnesium, and that repeated exposure to these conditions

decreased the level of oxygen atoms found in graphite. Eventually, the oxygen level was found to be 0% for MS5 samples.

4.6 XPS

XPS analysis was done to further corroborate elemental analysis from EDX. Spectrum analysis was done using the CasaXPS software and then plotted using the python matplotlib module. The XPS analysis was done on 2 sample types: 1) DG and 2) MS5.

Initially, a broad survey was done for both samples as shown in Fig. 20a, b over the range 1200eV to 0eV. Next the elemental analysis was narrowed to specific elemental signatures, specifically magnesium, carbon, and oxygen. The spectra over these ranges have overlays from the deconvolution of peaks in these locations.

The broad survey in Fig. 20a, is the broad survey for untreated graphite pallets. Fig. 20a is the low-resolution survey and only has two significant peaks, at 284eV it has a carbon peak and at 533eV it has an oxygen peak. Fig. 20b has the same major peaks and looks very similar in a low-resolution scan.

Fig. 20c and 10d are a high-resolution scan over the range 40eV to 60eV which magnesium. These peaks were incredibly low-resolution and noisy. It is unlikely that magnesium ions are deposited within the graphite palette. Since the graphite is additionally protected from the magnesium surface by filter paper during these tests, there is no contact between magnesium and graphite. The only means for magnesium deposition in the graphite is if magnesium hydroxide is dissolved in water and is left as the water flows out of the sensor and evaporates. Magnesium hydroxide is well known to have very low solubility in water, however, and is unlikely to dissolve. This is also consistent with the pH of water from the

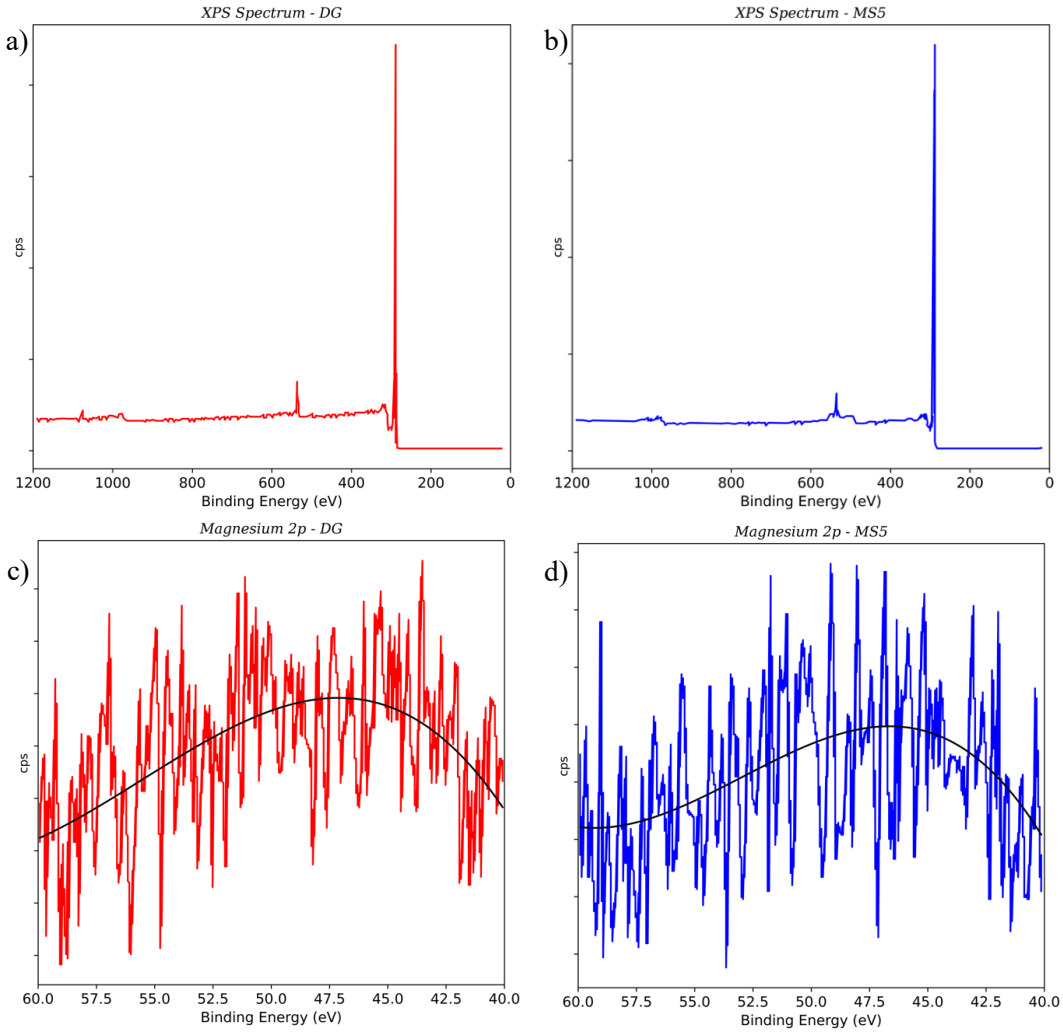


Fig. 20 a, b) Low resolution XPS spectrum sweep for DG sample and MS5 sample, cod) High resolution XPS spectrum from 40 to 60 eV to determine magnesium content in DG sample, and MG5 sample.

pre-analysis conditioning was also found to be at around 10, which is the maximum pH from magnesium hydroxide regardless of concentration due to its insolubility in water.

Fig. 21 shows the high-resolution scans over two ranges. Fig. 21 comprises of screenshots from the CasaXPS software displaying the material composition according to the peak deconvolution tool. First Fig 21a, b shows the range 522eV to 543 eV which is the primary region of O1s . The main oxygen peak is at 533eV, so it is likely that the small amount of

oxygen in the sample may be in organic C-O bonds [85]. These carbon-oxygen bond types are present in the structure of graphite oxide. This region may overlap with Na KLL, Sb3d, Pd3p, V2p peaks, however these elements are not likely to appear in this graphite analysis [86]. The peak deconvolution in this range showed 4 major peaks which were the same for both the DG and MS5 graphite. These peaks correspond with C-O bonds, C=O bonds, C-O-C/C-O-H, showing evidence of alkoxyl, ether and carbonyl groups which are commonly found on GO surfaces as dangling bonds [85]. There are differences between the DG and MS5 samples in the case of the proportion of different types of carbon-oxygen bonds. The MG5 has more carbonyl groups by a small percentage. Fig. 21c, d is a high-res scan on carbon is a 278eV to 297eV and gives information about the C1s carbon atoms in the sample. According to the peak deconvolution the carbon peak was separated into 3 individual peaks at around 284, 285, and 286. The most dominant peak is at 284 for both samples which is the C-C alkyl bond. The C1s region is asymmetric with a low intensity, broad peak on the side of higher binging energy. This is a satellite feature that is present in samples with high concentrations of sp^2 carbon, such as graphite. This is represented on the XPS in Fig. 12, as the pi-pi bond peak. Comparing the deconvolution of peaks around C and O to literature shows that the smaller carbon peak at 286eV appears to represent a C-O-C bond [85]. Additionally, there is a small peak at 288eV in the literature that arises due to O-C=O bonding. Around oxygen the peaks in literature occur at 531.5eV (representing organic C=O bond) and 533eV (representing organic C-O bond).

In addition to the peak deconvolution, a ratio of C-C to C-O the bonds ($I_{c\text{-}c/c\text{-}o}$) can be determined from the C1s range. Since the absolute XPS intensity tends to vary from sample to sample, this determination is very valuable in evaluating oxidation level. It is found that for the DG sample, the $I_{c\text{-}c/c\text{-}o}$ is around 0.39 and in the MG5 sample, the $I_{c\text{-}c/c\text{-}o}$ is at 0.31. This

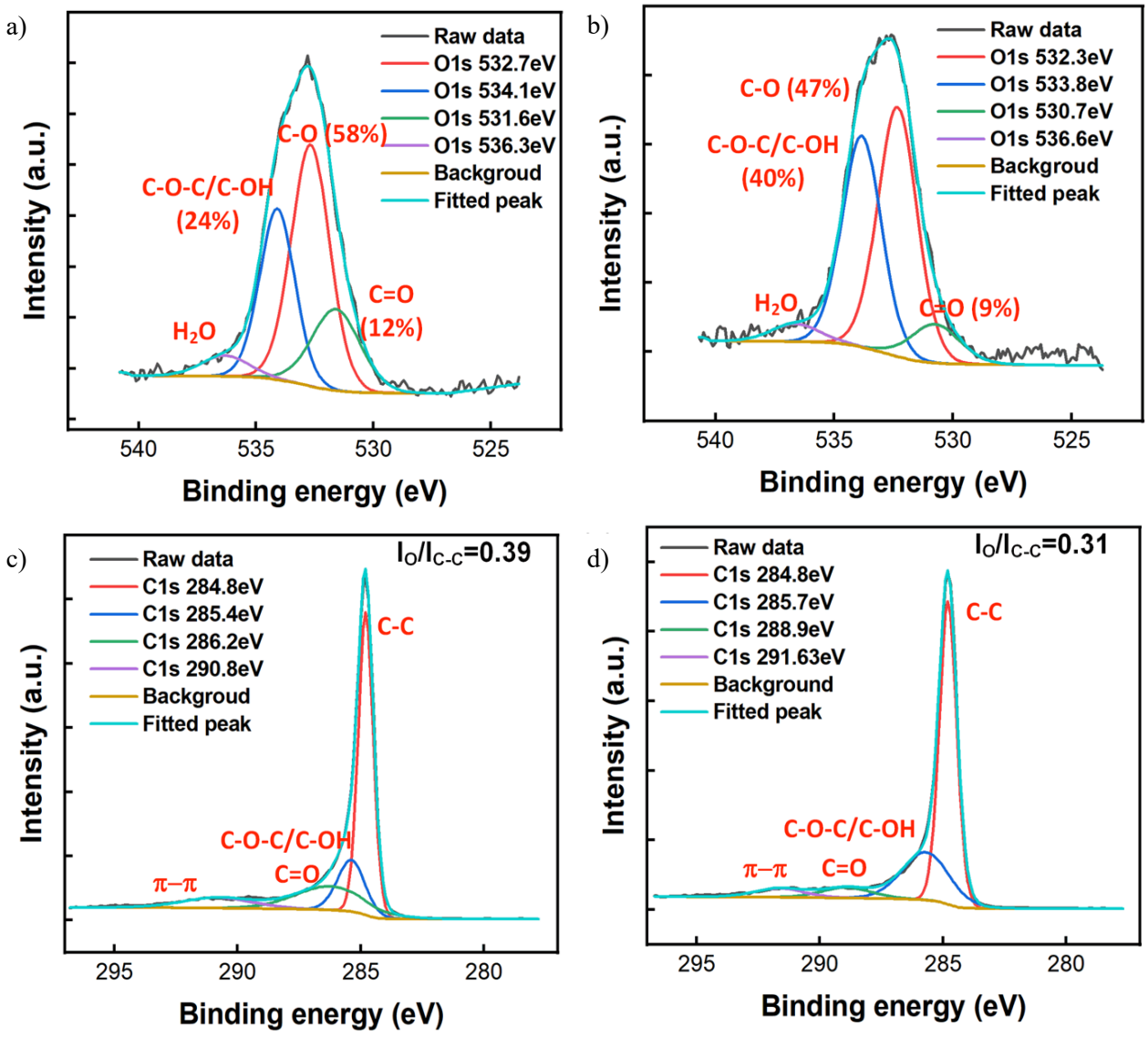


Fig. 21 a,b) Low resolution XPS spectrum sweep for DG sample and MS5 sample, c,d) High resolution XPS spectrum from 40 to 60 eV to determine magnesium content in DG sample, and MG5 sample.

indicates a significant decrease in oxygen content in graphite. It appears as though the overall sensor function consumes oxygen atoms from the graphite palette.

In conclusion, the XPS data analysis reveals that the elemental analysis is consistent with EDX. Oxygen seems to be consumed in the voltage generating reaction. This reaction was previously thought to be exclusively between magnesium and water, with the graphite palette being the location of the cathodic reaction, however, there may be a small contribution to this reaction from a graphite reduction reaction that would be explained by the consistent decline in oxygen content displayed by these XPS results.

4.7 Raman

The graphite layer was further characterized using Raman spectroscopy. The samples tested were divided into 4 categories with 5 samples each. These categories are as follows:

a. Dry graphite samples (DG)

b. Graphite samples exposed to water on glass slides (GS)

c. Graphite samples exposed to water on magnesium sheet (MS)

d. Graphite samples exposed to water on magnesium sheet 8 times (MS8)

Raman spectra was performed using a green 532nm laser. Since Raman spectra are collected from a small volume, up to a depth of 10μm [87], it is important to note that the analysis is done on the surface of the graphite. In the samples that were exposed to water, the surface that was in contact with glass or magnesium were analyzed. The Raman spectra literature shows GO and graphite on the transformation from graphite to graphene oxide required oxidation process. There were structural changes during the chemical process from graphite to graphene oxide. The Raman spectra for graphite had D-band at wavelength of 1328 cm-1

and G-band at 1573 cm-1 [65]. While for GO, the D band at 1324 cm-1 and G band at 1599 cm-1 [65].

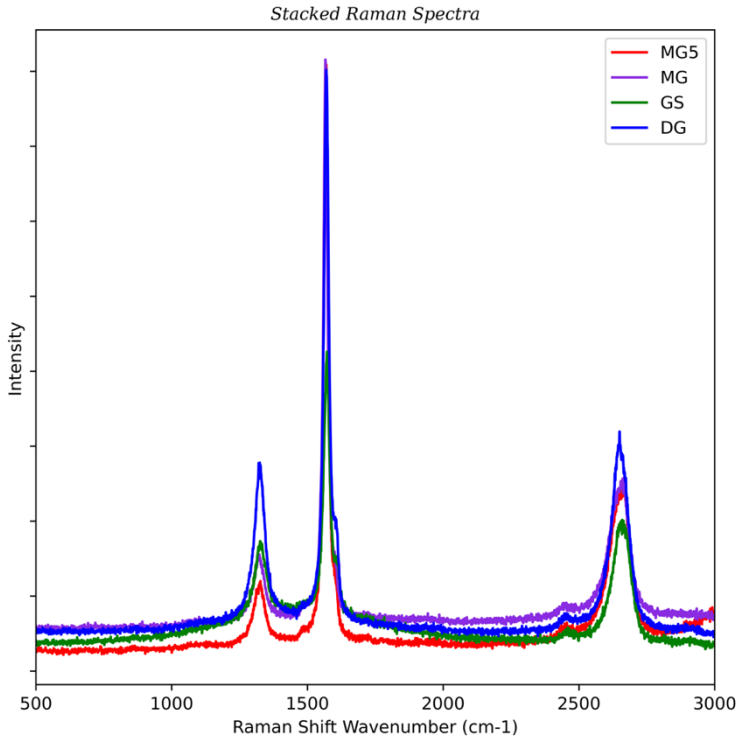


Fig. 22 Raman Spectra overlay for graphite samples in 4 conditions: DG, GS, MS, MS5

The Raman spectra for graphite in each condition is overlayed in Fig 22. In this image it is clear that there are 3 main graphite peaks that are located at 1325cm-1, 1600cm-1, 2650cm-1. They are typically associated with the D band, G band and 2D band respectively. There are also some clear shifts and changes in the peaks as the graphite condition is changed. In order to analyze the Raman spectra more closely, they were separated into ranges around the three peaks as seen in Fig 23. Additionally, the average peak locations as well as peak ratios are shown in Table 5.

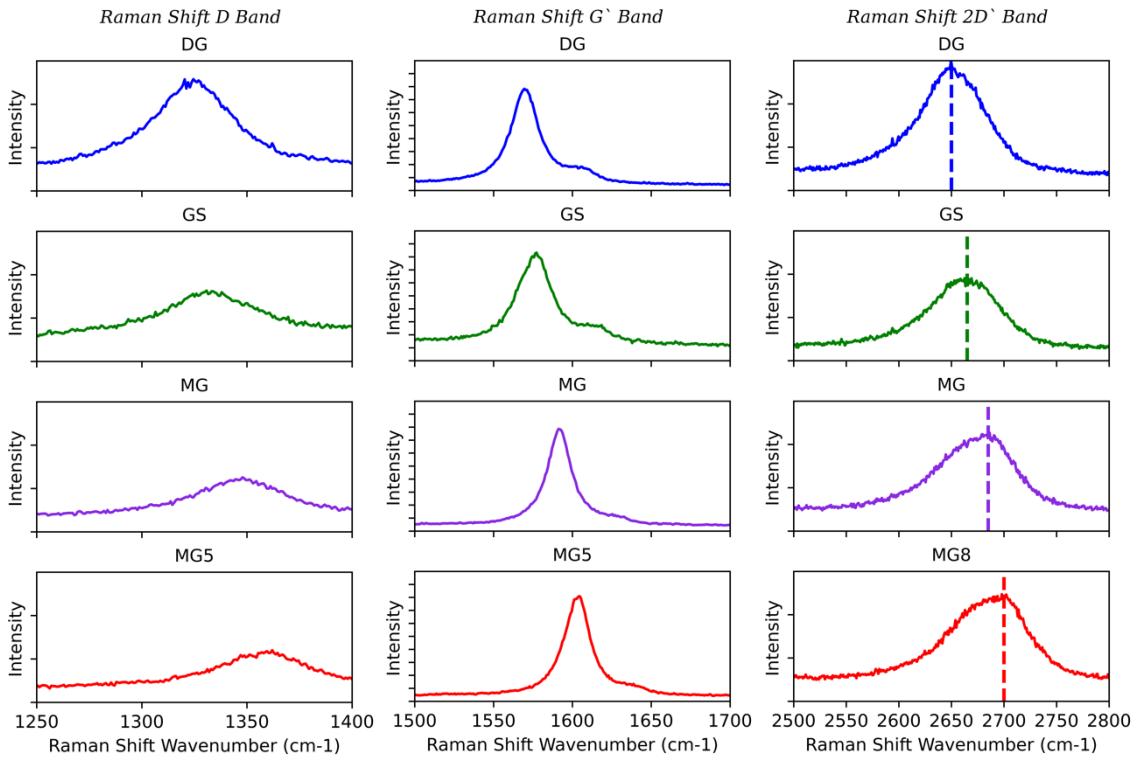


Fig. 23 Raman bands a) D band locations, b) G band locations, c) G' band locations

In many spectroscopy techniques, the absolute intensity of the peak is extremely variable, and therefore, peak ratios are much more valuable information to compare spectra. In this case one ratio gives information about the oxidation level of the graphite. The D/G ratio is well known to correspond inversely to the elemental C:O ratio. The D/G ratio is the most significant marker of graphite defects, with a higher D band indicating more defects.

The G band is associated with the 2p configuration of carbon that is associated with graphite and is resonant. Therefore, it is typically the dominant band in graphite samples. The G band location can often give information about the number of layers of graphene, however, since all the samples tested have the same general scale of graphite particles, no significant changes were detected. This small shift may indicate that the graphite involved may have some characteristics of graphene.

IN these samples there is a clear trend as seen in Table 5 where the DG and GS samples have the highest D/G ratio followed by MS, and MS5 samples. The GS sample had the highest D/G ratio overall, which may indicate that it has the highest oxygen content. IF this is true, the exposure to water alone may not increase the oxygen content in graphite. However, MS and MS5 having the lowest D/G ratio indicates a reduction in oxygen content further supporting that there seems to be an effect of consumption of oxygen through reduction in the graphite cathode that is specifically involved in the power generation reaction.

Another indicator of oxygen level is the 2D band location. This band is typically located at 2650. The 2D band experiences a shift to the right over the 4 conditions. The 2D band starts around 2659cm-1 for the DG sample and shifts progressively right from GS to MS to MS5. This is also associated with decreasing oxygen content in literature.

Table 5: Raman peak locations

Sample	D Band Location	G Band Location	2D Band Location	D/G	G' band shift
DG	1333.2	1574.5	2658.9	0.33364182	1084.4
GS	1333.2	1575.4	2669.8	0.38685103	1094.4
MG	1329	1573.7	2678.9	0.25652815	1085.2
MG8	1325.7	1569.5	2682.6	0.14002656	1091.1

4.8 Summary

Initially, the role of graphite in the sensor was relegated to a water wicking agent that was also conductive. In this chapter the graphite was treated to 4 conditions: 1) dry graphite, 2) graphite exposed to water, 3) graphite exposed to the full redox reaction, and 4) graphite exposed to the redox reaction multiple times.

It was characterized using SEM, EDX, XPS and Raman analysis to evaluate its structure and composition. The EDX results showed a significant decrease in oxygen content in the graphite. This was supported across these characterization methods. It is clear that the graphite has a lower oxygen content as it is involved in the redox reaction of magnesium at the cathode. The role of graphite in the sensor seems to be that of reduction and to provide a source of readily available oxygen atoms.

Chapter 5
Effect of Environmental Conditions on Sensor Function

5.1 Introduction

This chapter is focussed on the sensor's practical use in multiple environments. As stated in Chapter 2, the sensor function is determined by a process that is both unpredictable and uncontrollable. Additionally, as stated in chapter 3, the sensor must reach an initial maximum voltage of 1.5 V in order to activate the electronics successfully. The 2 main conditions of sensor failure are 1) the sensor voltage does not reach 1.5V while a leak is occurring or 2) if the sensor voltage exceeds 1.5 volts when there is no leak. In this chapter the sensor behaviour is evaluated across 3 main environmental conditions and additionally in a sensor aging test.

The plurality of water leaks sensors on the market have entirely electronic components and PCBs that can easily have lifetimes that range decades [90], the material characteristics of these sensors are not a significant problem. Contrastingly, the materials-based sensor in this work is powered by a corrosion reaction. Therefore, the materials-based system, while having the advantage of being self-powered, is much more variable performance over time.

5.2 Temperature Effects

The first condition tested is a temperature test. First, the material stack alone was exposed to the temperature condition, then the packed sensor was put in the same conditions to determine the effect on sensor performance and if the packaging resulted in different performance.

This test was carried out across 5 temperatures with n=5. The temperatures were 5°C, 10°C, 25°C, 35°C, 70°C. The temperatures were limited on the upper and lower ends by the temperature where liquid water could remain consistently. The sensors were kept at these

temperatures for 8 hours before each test either in a freezer or oven. To prevent condensation affecting the sensors they were vacuum sealed before being exposed to temperature differences. The temperatures were checked repeatedly with an IR thermometer to keep the range within 5°C of the intended temperature over the duration of the conditioning. Additionally, the temperatures were verified prior to exposing the sensors to water.

5.2.1 Materials Only Test

The materials only test involved the magnesium sheet, filter paper and the graphite piece. The results of this test can be seen in Fig. 24 . Fig. 24a shows the average plots of the materials only test at each temperature. Fig 24b plots the average maximum plot against temperature with calculated standard deviation to show the data spread.

As shown on the graph below, for all temperatures the sensors would have activated the beacon as they all reached a maximum voltage between 1.84V to 2.10V. In the materials only test, the samples 25°C were able to reach the highest maximum voltage on average. The samples at 35°C and 70°C had similarly high average maximum voltages. The effect of the colder temperatures was much larger, seeing a drop in max voltage of 0.21V for 10 and 0.22V for 5 and 10°C.

It also seems that the test at 5°C and 10°C take more time to get to the max but the difference between the results for each temperature stays minimal and negligible.

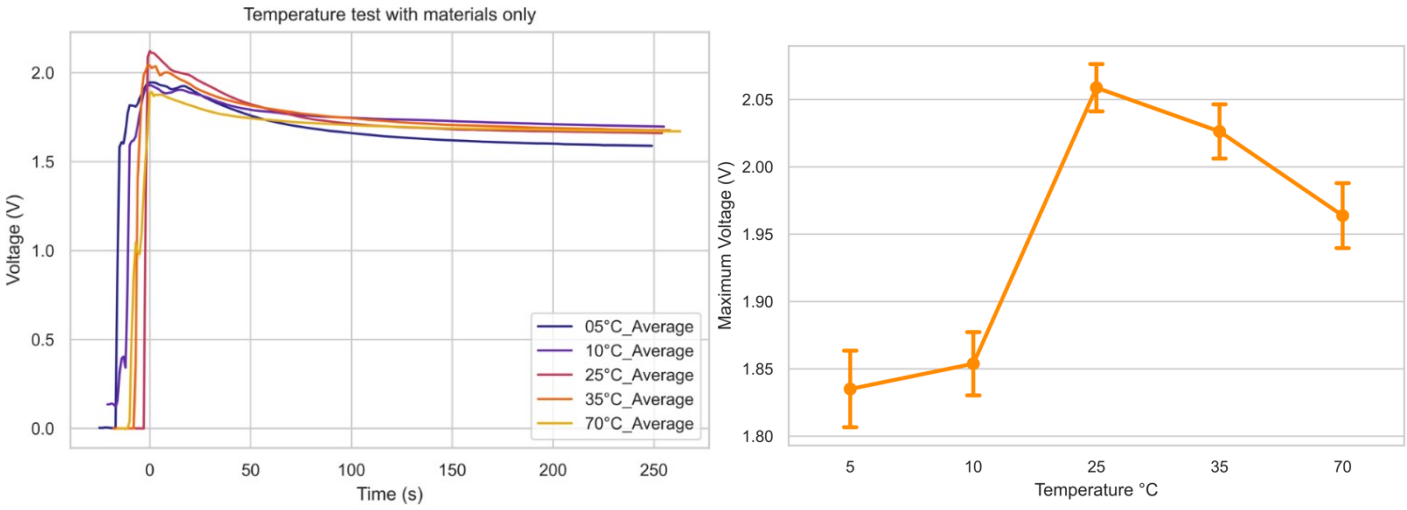


Fig. 24 a) Average load test voltage characteristic (n=5) for materials only samples over each temperature. b) Average maximum voltage plotted against temperature.

5.2.2 In Package Test

A similar test was conducted yet in-package. This test kept the temperatures much more stables. In this setup, the samples were submerged into water at the specified temperature. Consequently, the following graph (Fig25) displays more variability overall as indicated by the standard deviation bars on Fig 25b.

Interestingly, the spread in the time it takes to reach the maximum voltage is exaggerated for the colder temperatures as visible in Fig 25b. This may be because the entire package has an insulating effect and so it returns to the equilibrium temperature of the room much faster. This study was also used to gauge the sensor behaviour at near body temperature for expansion of the scope of this sensor. As shown in Fig25 for all temperatures the sensors would have activated the beacon as they all reached a maximum voltage between 2.0V to 2.15V. However, the tests at 25°C were able to reach the highest max voltage and were the quickest to reach it on average. It also seems that the test at 5°C and 10°C take more time to get to the max but the

difference between the results for each temperature stays minimal and negligible. According to the first experiments, the effects of temperature weren't significant and wouldn't affect the performance.

It has been seen in literature that the corrosion reaction of magnesium is heavily affected by temperature. Elevated temperature is seen to accelerate corrosion in water. This is common for many corrosion processes. In this case

The temperature conditioning did not have a significant effect on overall sensor function as every sensor crossed the minimum voltage threshold of 1.5V for long enough to be able to activate the electronics. However, since this effect is accelerating corrosion at higher temperatures, and slowing corrosion at lower temperatures, it is likely that there may be an effect on the repeatability of the sensor. This may be an effect of the thickness of the magnesium passivating layer changing as the sensors are kept at different temperatures.

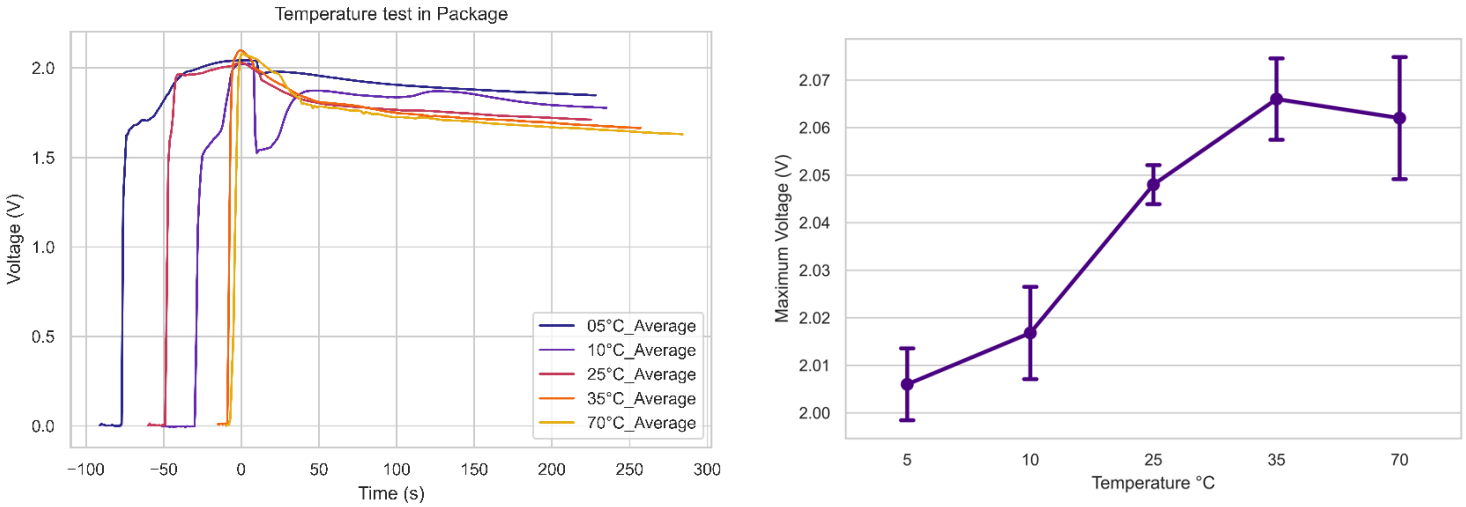


Fig. 25: a) Average load test voltage characteristic (n=5) for materials only samples over each temperature. b) Average maximum voltage plotted against temperature.

5.3 Humidity Effects

The humidity tests were also split into two categories: first materials-only and then in- package. This clearly determined the effect of humidity on the materials themselves and then observe if the packaging of the sensor provides any protection for the sensors. Humidity is another environmental condition that changes with location and season. Since humidity is an evaluation of the water The water that can be suspended in air is heavily dependent on the temperature of the region. For the duration of the humidity tests, the temperature is also monitored by the same device and was found to range from 23 to 24. The setup of the humidity test can be seen below in Fig 26. A sealed humidity chamber was created in which the samples were kept for the duration of this test.

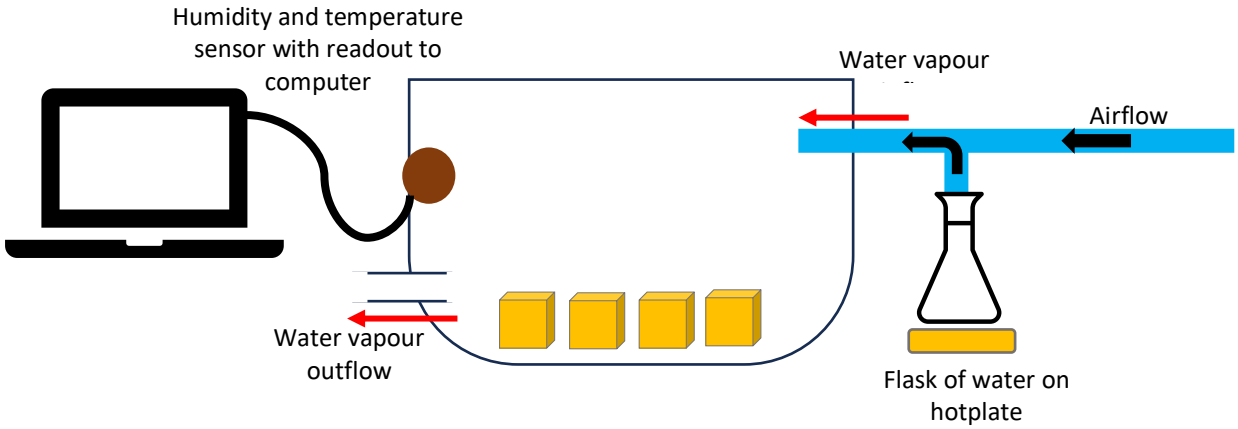


Fig. 26: Humidity chamber setup for retaining 85% humdity

In order to create the water vapour, a flask of water was kept on a hotplate, so the water evaporated. This was connected to an inlet on the chamber using piping. This channel was also connected to the lab airflow to push the water vapour into the chamber. An outlet was created on the other side of the chamber in order to release the air pressure inside. Additionally, a humidity and temperature sensor were inserted into the chamber and displayed data on a

computer. The humidity level was calibrated by changing the temperature of the hotplate and the lab airflow through the tubing. The humidity level was monitored for one hour after setup to ensure that it was stable enough to introduce the samples.

The testing procedure in these conditions were to put samples in a high humidity condition for 3, 6 and 9 days with n=5 for both materials only and in-package testing. The samples were placed in a humidity chamber monitor to keep the humidity around 85%. The simulated humidity varied from 78% to 90% as reported by the humidity sensor. The samples were tested using the load testing procedure in Chapter 3. The voltage characteristic curves for materials only samples are shown in Fig. 27. The 3 days on which the sensors were tested are displayed with the standard results at 23-24°C and 20-40% humidity. There is a clear change in the sensors from standard humidity conditions. The samples are much less consistent than the standard conditions. In each plot, the voltage drop associated with applying the load varies greatly between samples from 0.05V to 0.3 V. It is also clear that the initial voltages of the sensors are affected by humidity in the materials only study.

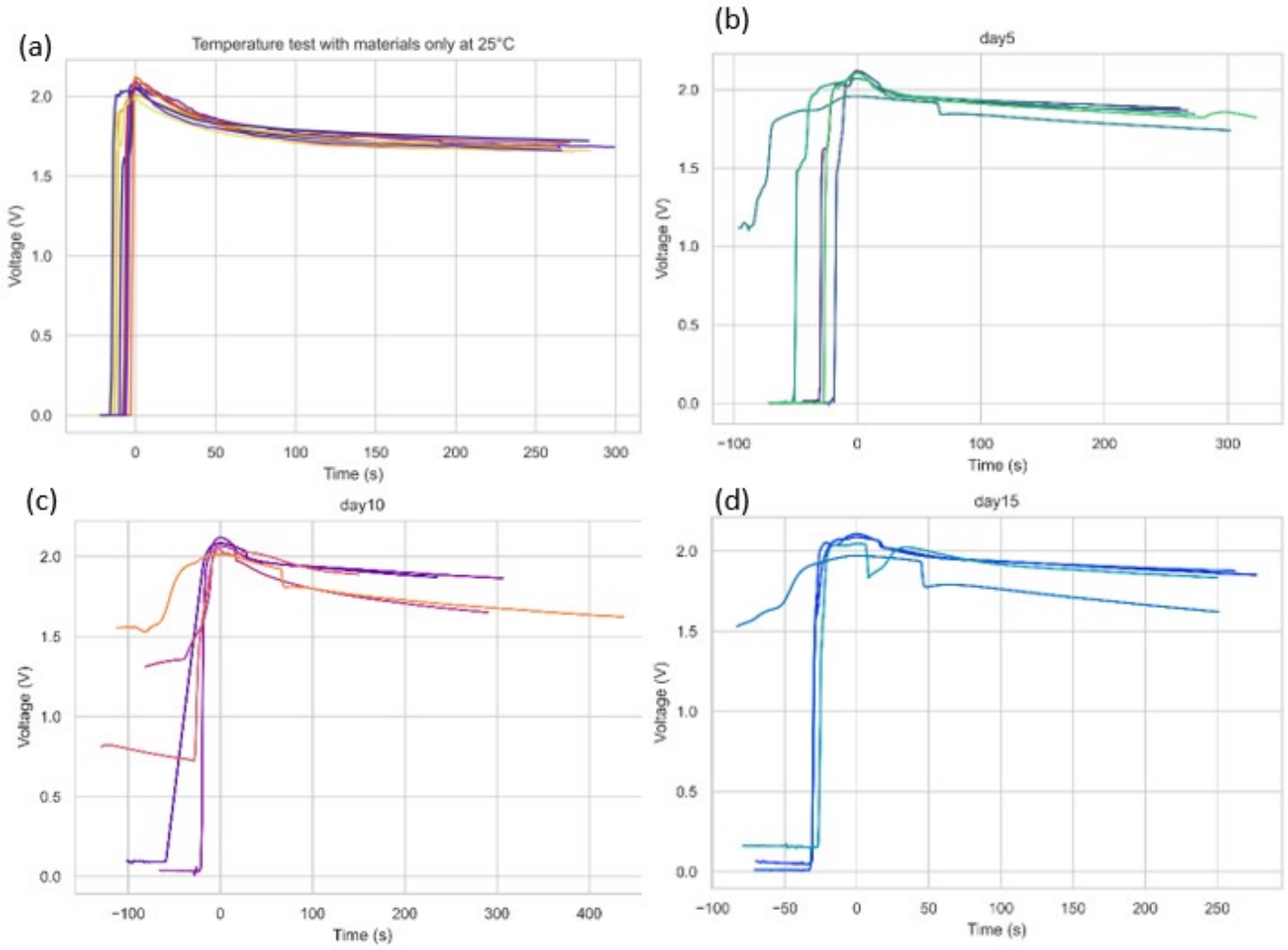


Fig. 27: Results for the humidity test for materials only samples: (a) reference at 25°C, (b) Voltage after 5 days, (c) Voltage after 10 days, (d) Voltage after 15 days

The in-package humidity results are displayed in Fig 28 . Similar changes can be seen on all three days in the voltage drop associated with the applied load. In these samples, the maximum voltage is also clearly affected and changes on average by 0.2V across all 15 samples. In contrast to the materials only samples, these samples did not show and change in the initial voltage and all samples started with 0V. One of the key evaluations in the humidity

test is the initial voltage. This is usually not considered because in all other tests, this value is 0V (or on the scale of μV). However, in the high humidity conditions this is a very obvious change in the materials only samples. On day 3, one sample has an initial voltage of 1.15V. On day 6, three samples have elevated initial voltage at 0.78V, 1.38V and 1.56V. Finally, in the day 9 group, one sample has an elevated voltage of 1.51V. Of the 15 samples, 3 would have resulted in false activation of the beacon. These variant samples did not seem to have differences in maximum voltage or extreme voltage drops when water was applied. Interestingly, this effect of elevcated initial coltage is not seen in the packaged samples. The fully exposed sensor materials with hygroscopic graphite appear draw in water droplets from the water vapour in the air at 85% humidity. There is a clear protective effect provided by the ABS packaging. While these samples were still clearly affected by high humidity over the duration of the test as seen in Fig, the effect is lessened and so does not cause sensor failure in general. There is no obvious trend that increasing the number of days at elevated humidity magnifies the effect on the samples in either the materials only or in-package samples. The source of variation in the results may be due to the sample's position in the humidity chamber.

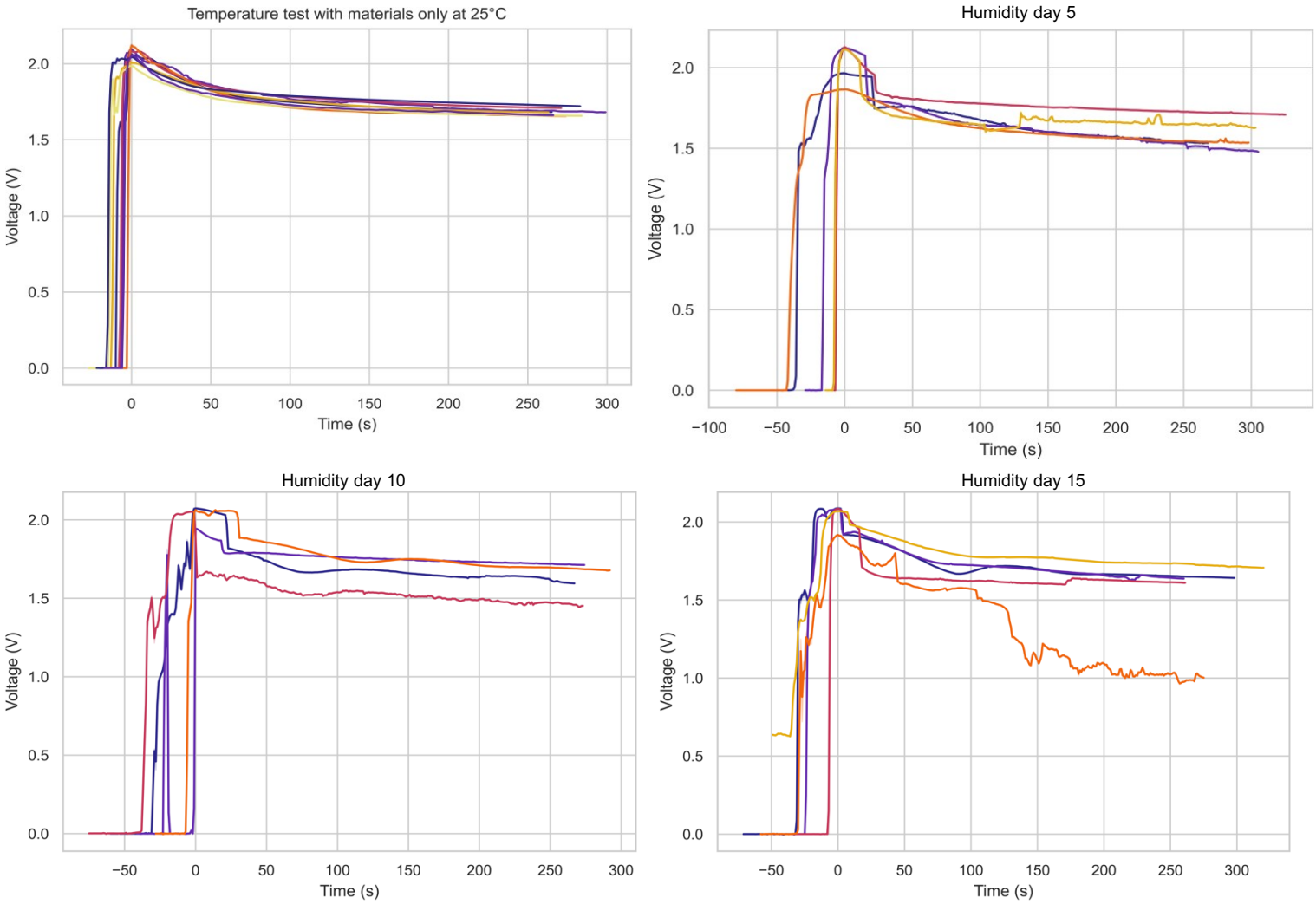


Fig. 28: Results for the humidity test for in-package samples: (a) reference at 25°C, (b) Voltage after 5 days, (c) Voltage after 10 days, (d) Voltage after 15 days

In conclusion, humidity has a significant effect on the overall performance of the materials stack. The materials only would have resulted in false activations 20% of the time after 6 days and up to 40% of the time after 9 days at around 85% humidity. This effect was mitigated effectively by the sensor packaging. Therefore, the sensors would not have been

activated in package after 9 days at 85% humidity. It cannot be said that there is no effect of humidity on packaged samples as the voltage drop caused by applying load is significant.

It is likely that the magnesium begins to corrode at this high humidity level as the voltage drops at the applied load. The initial voltage characteristic performs similarly to sensors that have been tested repeatedly. This indicates that the corrosion layer has begun to form and also that the repeatability of these samples will likely be affected.

5.4 Aging and Lifetime Testing

5.4.1 Accelerated Aging Testing

The samples in this study were kept in an oven at 100°C, 200°C, and 300°C with n=5. The samples were tested on 7,14, 21, and 28 days. These samples were materials-only because the ABS packaging would have melted at these temperature conditions. The samples were tested using the load test and the average power output over 4 minutes was calculated for each sample by multiplying the voltage output by the applied load of 50μA. These results were averaged and plotted in Fig. 30.

In Fig. 30 the first effect that is evident is that the power output decreases as the temperature increases. This is consistent on each day of testing. The second effect seen is that keeping the samples at the high temperature for a longer period of time results in a decrease in average power output. There is a clear decrease in the average power generated from day 7 to day 28 for all temperatures.

In general, these results may be a result of the oxidation of magnesium in air. The power producing reaction in the sensing materials is driven primarily by the conversion of magnesium to magnesium hydroxide as shown in Chapter 2. However, magnesium is also susceptible to oxidation in air according to the following equation:

$$Mg(s) + O_2\,(g) \longrightarrow 2MgO(s)$$

Magnesium tends to form a very thin oxidation layer in air like many other reactive metals. However, this reaction is well known to be affected by temperature. Magnesium metal can also react with oxygen in air to form magnesium oxide, which can occur at temperatures as low as 200°C [65]. At high temperatures, this reaction can occur more quickly and lead to a thicker layer of oxide forming on the metal surface, which can hinder its performance in some applications. At high temperatures, magnesium metal can be more susceptible to corrosion from certain chemicals or environments. However, the exact rate of oxidation will

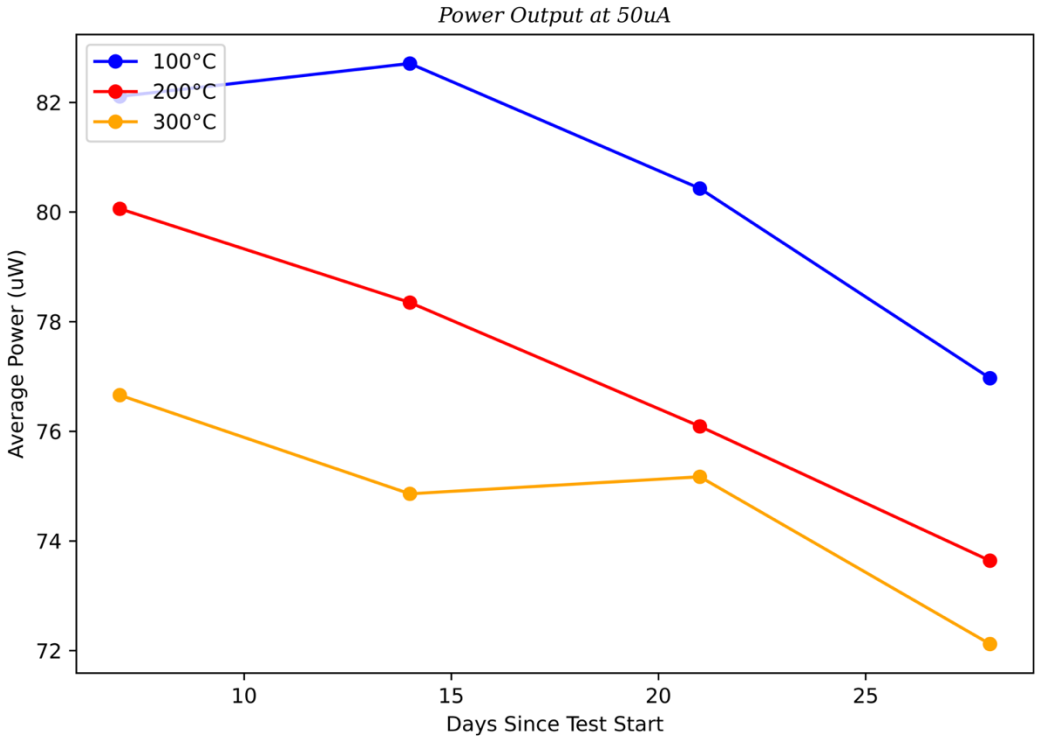


Fig. 29: Average power output after exposure to high temperature condition over 28 days

depend on several factors, including the purity of the magnesium, the surface area of the metal, and the environmental conditions in which the metal is stored.

5.5 Shelf Life: Long Term Viability of Materials Based Water Leak Sensor

The vast majority of water leak sensors on the market are based on closing a circuit using a drop of water. Since electronic components can last decades with no degradation, it is likely that these products have very long shelf lives. In the case of the materials-based sensor in this work, the materials are more susceptible to oxidation and water damage. The sensor itself relies on oxidation to generate power.

Several factors contribute to the shelf life of a product. These factors include moisture, mechanical stress, and heat. A product stored under low stress conditions may have a longer shelf life. Therefore, the storage atmosphere of a product contributes to the length of its shelf life [91].

The shelf-life test setup was initiated in June 2021 and completed in February 2023, running for a duration of 16 months. Samples were prepared and kept in the 2118A lab in the Engineering 3 building. They were kept on a shelf and 5 samples were tested in varying intervals. Samples were tested after 1, 2, 3, 4, 8, 12, and 16 months after the initial setup. The testing done was the standard load test described in chapter 3.

The effects of the 2-year shelf-life condition can be seen in Fig. 31. From the initial condition of the test to February 2023, the maximum voltage does not change significantly, as can be seen in Fig 31 a) and b). The main effect is in the power output which encompasses the voltage characteristic after the load is applied. There is clearly a large variety in the samples that are tested in Feb 2023, and the voltage drop caused by the load changes from 0.15V to 0.5V.

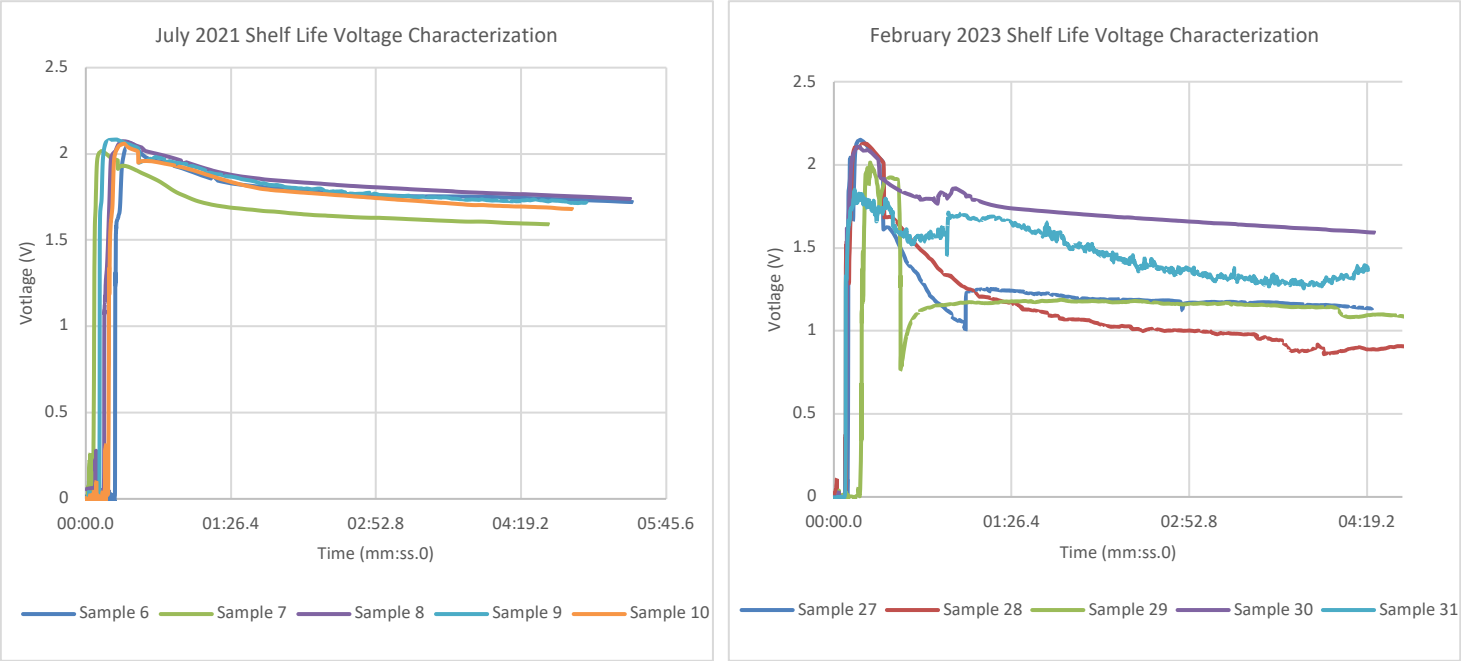


Fig. 30: Shelf Life 1 month (July 2021 vs February 2023). In July 2021, the behaviour of the fresh sensors is much closer to fresh sensors, there is a visible difference.

5.5.1 Sensor Voltage Mapped with Monthly Absolute Humidity

From the shelf-life plots, the power over 4 minutes was calculated by multiplying the voltage after the load is applied by the 50µA applied. The shelf-life results were averaged and analyzed over the 16-month duration. It is clear that there is a change in power generation over time. Magnesium that has exposure to moisture and other environmental factors can lead to corrosion and degradation of the alloy over time.

Based on the previous Temperature or Humidity states – since it is a water-based sensor, it needs to be water related and the temperature has a huge effect on atmospheric humidity. Plotting the Shelf-Life Behaviour over time reveals what looks like a twostep drop in maximum voltage. Since this occurred over time, observing where the drops have occurred reveals that the two local minima are both in October of 2021 and 2022 (4 and 16 months).

This suggests some investigation into climate effects on the sensors. Since it is well known that humidity has a substantial effect on sensor performance both for the materials only and for the fully packaged sensor, it is likely that long term climate is affecting the sensors as well.

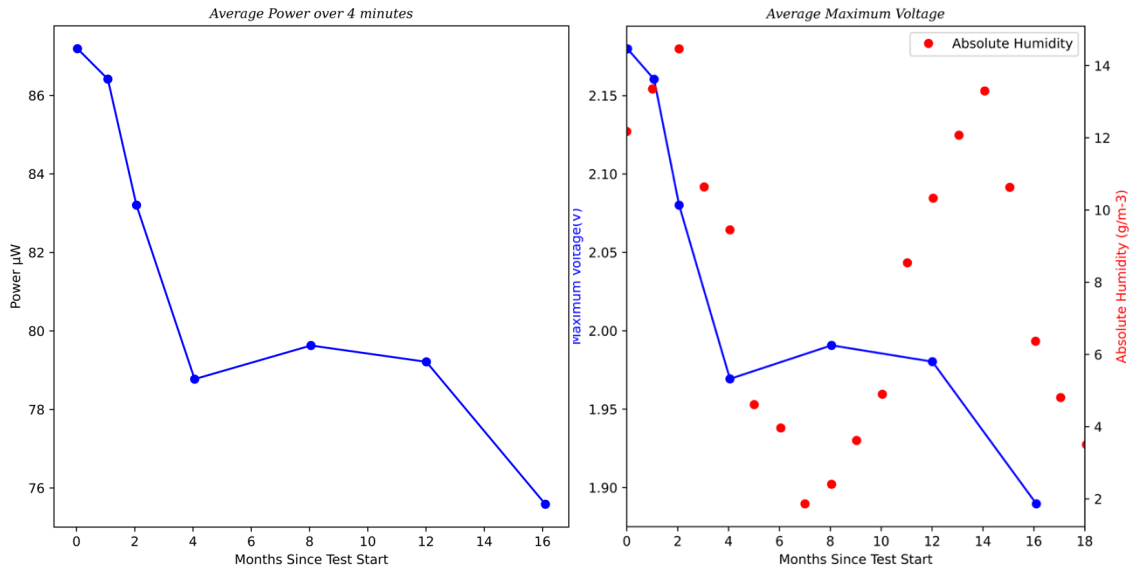


Fig. 31: a) Average power of packaged shelf life samples over 16 months, b) average power of shelf-life samples over 16 months, plotted with monthly absolute humidity.

Absolute humidity measures the mass of water vapour present in a given volume of air. On the other hand, relative humidity is the amount of water vapor present in the air expressed as a percentage of the maximum possible amount of water vapor that the air can hold at a given temperature. Absolute humidity does not consider the air temperature and only depends on the amount of water vapor. However, most climate data is reported in terms of relative data, so the relation between absolute and relative humidity is as follows. Using relative humidity data, and air temperature, we can calculate the absolute humidity in g/m^3 using the equation:

$$AH = \frac{RH \times Ps}{Rw \times T \times 100}$$

Variables: RH: Relative humidity, Ps: pressure, Rw: Specific gas constant for water vapor, T: temperature in Kelvin.

In Fig. 32b, the average power is plotted against the calculated absolute humidity. The monthly average humidity was used from the Kitchener-Waterloo Weather Dashboard [92]. The two-step drop is found to follow periods of high humidity.

5.6 Summary

This chapter explores the effect of environmental conditions on the sensor performance, primarily by investigating the load test results of each sample. The sensors were first tested across a temperature range (5°C – 70°C) in which it is observed that sensors achieve higher maximum voltage at high temperature. Next the effect of elevated humidity was determined to increase the initial voltage of materials only samples and expand the voltage drop for packaged sensors. The aging of the sensors was also tested. First an accelerated aging test was performed by exposing the sensing materials to temperatures (100°C to 300°C) to simulate accelerated oxidation in air. This oxidation had a negative effect on sensor load tests. Finally, a 16-month shelf-life test was reported. This real time aging test had a significant effect on sensor power output, and it is likely that this behaviour is linked to local humidity conditions.

Chapter 6

Development of a Graphite Composite for Improved Sensor Resilience

6.1 Introduction

The graphite palette is made of a mix of powders compressed at 100N in the Instron 5548 micro tester. This results in a very fragile material that breaks easily upon use. Breaks in the material slow the flow of water. Since the water is drawn up through pores in the material that act as a bundle of parallel capillary tubes, cracks in the material create "pores" or gaps larger than the capillary length. This, according to Jurin's Law [93] prevents the capillary rise in the graphite palette which in turn slows the redox reaction as it reduces the contact of water with the Reactive Layer.

To address this issue, the graphite palette powder mixture is encased in a polyvinyl alcohol (PVA) matrix to make a graphite palette-composite piece. This composite piece can be made at different proportions of graphite palette: PVAc and differing compression force. In order to allow for the diffusion of water, each piece must retain its porosity in the polymer matrix.

From initial experiments it was determined that the compression force is an important factor in creating a strong enough piece, but also affects the porosity [94]. Increasing the compression force increases the strength of the piece whereas, not enough compression will result in a crumbly graphite palette that will break easily. Additionally, the compression force is inversely proportional to the porosity, so maximizing the compression force will result in a graphite palette that is impermeable to water, which would prevent the power generation.

The ratio of graphite pallette:PVAc is also a factor that effects power generation. Increasing the ratio of graphite pallette:PVAc results in a more conductive piece (improving power generation), since the graphite palette powder is conductive and the PVAc is insulating. However, adding PVAc and decreasing the ratio of graphite pallette:PVAc results in a more robust piece that is less likely to crack.

6.1.1 PVAc - Graphite Composite: Response Variables

Both the graphite pallette:PVAc ratio and the compression force affect the electrical performance of the system and are input parameters in this statistical analysis. The effect on electrical performance was confirmed from initial experiments [94]. The electrical

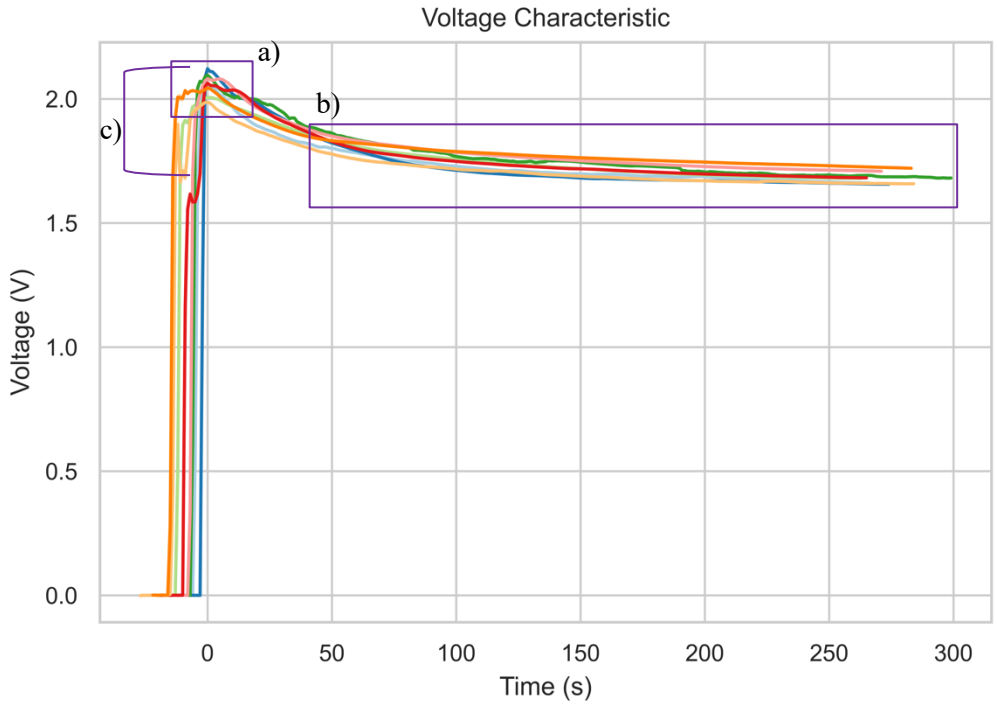


Fig. 32: Example raw data with a) maximum voltage, b) average power over 150s, c) voltage decay

performance can be measured as three response variables: the maximum voltage, the average power generated in 150 seconds, and the rate of voltage decay (see Fig. 2)

These three signals are all extracted from the raw data which is measured using a digital multimeter. The specific equipment used is:

Table 6: Equipment Models and Accuracy

Equipment	Model	Accuracy
DMM	Agilent34401A	0.0035%
Power Source	Agilent b2911A	0.02 %
Micro tensile tester	Instron 5548 micro tester	0.4 %

A Summary of parameters and response variables is as follows:

Input parameters:

1) compression strength (N),

2) ratio of graphite palette: PVAc (wt.%)

Response variables:

1) Maximum voltage abbreviated as max.V.(V),

2) Average power generated over 150s (μW),

3) Rate of voltage decay abbreviated as dV/dt (mV/s)

6.2 Statistical Analysis of Response Variables

The goals of this statistical analysis are to identify relationships between the parameters (compression force and graphite pallette:PVAc ratio) and response variables (maximum voltage, power generated, voltage decay) using Minitab Statistical Software [95]. First Minitab is used to design the experiments. Next, since both input parameters are continuous,

the ANOVA method is used to compare the means of the response variables at more than 2 parameter levels.

6.2.1 Design of Experiments

The design of the experiments was based on the initial experiments varying graphite pallette:PVAc ratio and compression force. The Minitab DOE module was used to design the experiment using the central composite design for a 2-factor system. Central composite design [95] was chosen because it is best suited to the response surface methodology and because it functions with only two input parameters.

The CCD cube points were determined from previous data and the axial points were generated using Minitab (Table 2). The experiments were conducted in a randomized order from Minitab with 5 replicates.

Table 7: Coded Parameters for CCD and Real Values

Points	Coded Parameters	Compression Strength (N)	Graphite:PVAc (wt%)
Axial	1.41421	38.8	60.8
Cube	1	75	65
Central	0	162.5	75
Cube	-1	250	85
Axial	-1.41421	286.2	89.1

6.2.2 One Way ANOVA

The one-way ANOVA and regression will be used to analyze the relationship between each response variable and the effect of the two input parameters in each case. ANOVA was chosen (instead of t-tests) because each parameter has more than two levels tested.

For this analysis, a significance level of 0.05 was chosen. P-values above this alpha mean that the null hypothesis (H_0) should be accepted, and p-values below this alpha reject the null hypothesis and accept the alternative hypothesis (H_A). In this section, the null and alternative hypotheses are:

H_0: all means across each factor level are equal.

H_A: all means across each factor level are not equal

Since the ANOVA only differentiates if means at all levels are different or not, the Tukey.

6.2.3 Maximum Voltage

The one-way ANOVA for the relation between compression and max. voltage gave a p-value much lower than $\alpha = 0.05$. The R^2 for this relationship is 0.79 indicating that the model explains a moderate proportion of the data. This can also be seen in the scatter plot in Fig. 3a. When analyzing the relationship between the graphite pallette:PVAc ratio and max.V., the ANOVA also resulted in a p-value lower than 0.05, however the R2 was significantly lower at 0.49 (visible in Fig. 3b). In the ANOVA, it is notable that the adjusted sum of squares value is greater for the error analysis than the parameter analysis. This indicates that the residuals present are not well explained by the graphite pallette:PVAc ratio.

The R2(adj) for both parameters is very close to the R2, which points to the low number of parameters in relation to the number of samples tested. Finally, Minitab has a Sequential ANOVA module that calculates the p-value for linear, quadratic, and cubic fits. The sequential ANOVA for compression confirms that the quadratic regression fit is better than

linear or cubic since it has the lowest p-value, and the only p-value under 0.05. The sequential ANOVA for graphite pallette:PVAc ratio.

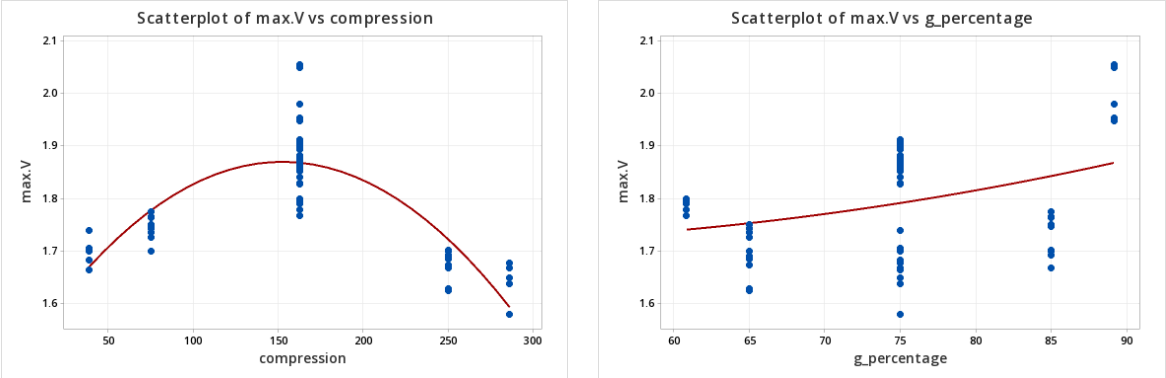
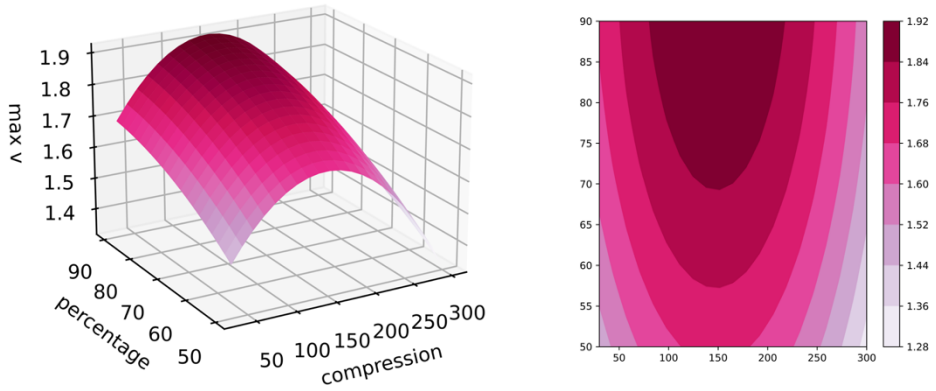


Fig. 33 Max. Voltage scatterplots with best fit curves

In the response surface ANOVA for the max. V. response variable, the R2(adj) for the surface was relatively high (Fig. 7) at 0.82, indicating strong correlation between the parameters and response variables. The p-values for the linear and square compression terms were less than 0.05 as well as the linear and square graphite pallette:PVAc ratio. The interaction terms and square graphite pallette:PVAc ratio terms both had p-values much greater than 0.05 and so were rejected in the final model.



Analysis of Variance

Source	DF	Adj SS	Adj MS	F-Value	P-Value
Model	4	0.604091	0.151023	71.99	0.000
Linear	2	0.109425	0.054712	26.08	0.000
compression	1	0.029395	0.029395	14.01	0.000
g_percentage	1	0.080030	0.080030	38.15	0.000
Square	2	0.494666	0.247333	117.90	0.000
compression*compression	1	0.493204	0.493204	235.11	0.000
g_percentage*g_percentage	1	0.002883	0.002883	1.37	0.246
Error	60	0.125865	0.002098		
Lack-of-Fit	4	0.085718	0.021430	29.89	0.000
Pure Error	56	0.040147	0.000717		
Total	64	0.729956			

Fig. 34: Max. Voltage: a) ANOVA table, b) Regression table, c) surface plot, d) contour plot

The lack of fit p-value is less than 0.05 which means that it cannot be said that there is no lack of fit. When the rejected model terms were removed, the lack of fit F-value improved, however there is still some significant lack of fit in the model.

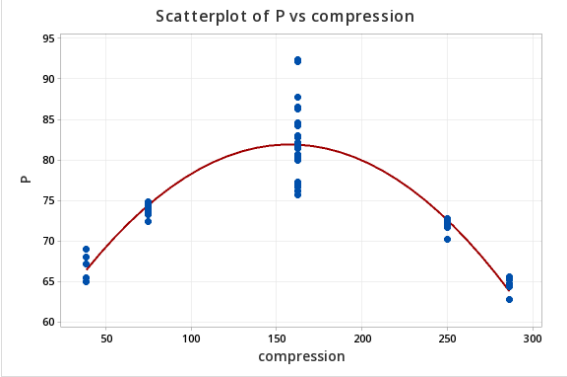
6.2.4 Power Generation

The one-way ANOVA for the relation between compression and power resulted in a p-value much lower than $\alpha = 0.05$. This relationship was fit with a quadratic regression model from the Sequential ANOVA where the p-value for the quadratic fit was the only one below the alpha value of 0.05. This fit had an R2 of 0.83, indicating a strong correlation between compression strength and power (Fig. 4a).

The one-way ANOVA for the graphite pallette:PVAc ratio resulted in a p-value lower than 0.05, but the R^2 value of 0.31 indicated a very weak correlation. This was fit with a linear regression model.

Similarly, to the max. V. behaviour, the adjusted sum of squares value is greater for the error analysis than the parameter analysis. This indicates that the residuals present are not well explained by the graphite pallette:PVAc ratio.

a



b

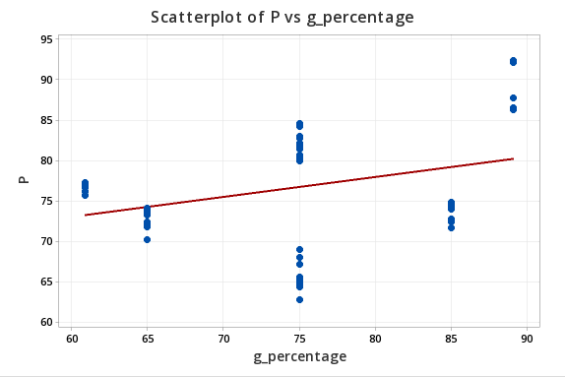


Fig. 35: Power scatterplots with best fit curves

In the response surface ANOVA for the power response variable, the R^2(adj) for the surface was high (Fig. 8) at 0.90, indicating very strong correlation between the parameters and response variables. The p-values for the linear and square compression terms were less than 0.05 as well as the linear and square graphite pallette:PVAc ratio. The interaction terms and square graphite pallette:PVAc ratio terms both had p-values much greater than 0.05 and so were rejected in the final model, similar to the max. voltage.

When the rejected model terms were removed, the lack of fit F-value improved, however there is still some significant lack of fit in the model due to the low lack of fit p-value.

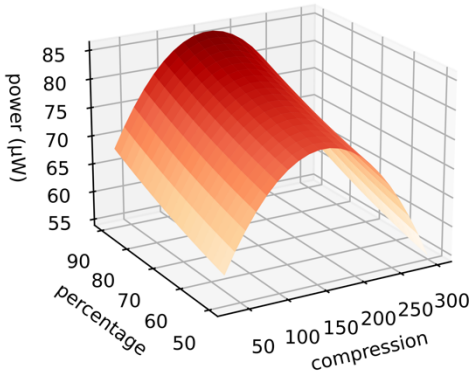
a **Analysis of Variance**

Source	DF	Adj SS	Adj MS	F-Value	P-Value
Model	3	2749.54	916.51	199.97	0.000
Linear	2	275.75	137.88	30.08	0.000
compression	1	34.55	34.55	7.54	0.008
g_percentage	1	241.20	241.20	52.63	0.000
Square	1	2473.79	2473.79	539.76	0.000
compression*compression	1	2473.79	2473.79	539.76	0.000
Error	61	279.57	4.58		
Lack-of-Fit	5	171.18	34.24	17.69	0.000
Pure Error	56	108.39	1.94		
Total	64	3029.11			

b **Model Summary**

S	R-sq	R-sq(adj)	R-sq(pred)
2.14083	90.77%	90.32%	89.34%

c



d

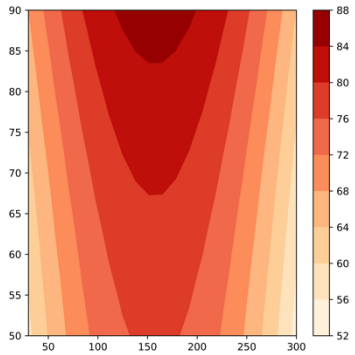


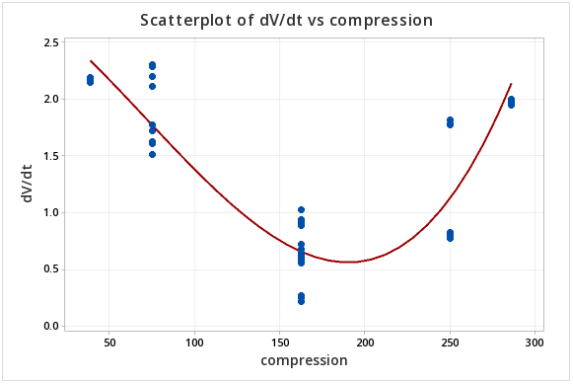
Fig. 36: Power: a) ANOVA table, b) Regression table, c) surface plot, d) contour plot

6.2.5 Voltage Decay

The analysis of the voltage decay data is similar to the analysis for the max.V. and power. The one-way ANOVA for the relationship between compression and voltage decay gave a p-value much lower than $\alpha = 0.05$. This relationship was fit with a quadratic regression model in accordance with the Sequential ANOVA. This fit had an R2 of 0.85, indicating a strong correlation between compression strength and power (Fig. 5a).

When analyzing the relationship between the graphite pallette:PVAc ratio and voltage decay, the ANOVA also resulted in a p-value lower than 0.05, however the R2 was significantly lower at 0.37. Additionally, the adjusted sum of squares value is greater for the error analysis than the parameter analysis. This indicates that the residuals present are not well explained by the graphite pallette:PVAc ratio.

a



b

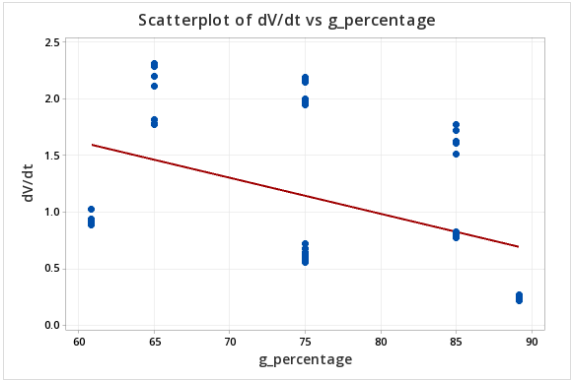


Fig. 37: Voltage Decay scatterplots with best fit curves

In the response surface ANOVA for the voltage decay response variable, the R^2(adj) for the surface was high (Fig. 9) at 0.93, indicating strong correlation between the parameters and power generation. All the linear terms, square terms and interaction terms have p-values less than 0.05 and were all included in the model. Finally, this model also included some lack of fit.

In the response surface, the R-squared values across each response variable indicated strong correlation between compression force and ratio and each response variable. The maximum voltage response surface indicates that the highest maximum voltage occurs at a graphite pallette:PVAc ratio of 89 as well add a compression of 165N this is apparent in the visual response surface as well as the contour plot where the peak can be visually estimated.

Analysis of Variance

Source	DF	Adj SS	Adj MS	F-Value	P-Value
Model	5	27.9657	5.5931	178.82	0.000
Linear	2	5.5810	2.7905	89.22	0.000
compression	1	1.5510	1.5510	49.59	0.000
g_percentage	1	4.0301	4.0301	128.85	0.000
Square	2	22.1923	11.0961	354.76	0.000
compression*compression	1	22.1268	22.1268	707.43	0.000
g_percentage*g_percentage	1	0.1295	0.1295	4.14	0.046
2-Way Interaction	1	0.1924	0.1924	6.15	0.016
compression*g_percentage	1	0.1924	0.1924	6.15	0.016
Error	59	1.8454	0.0313		
Lack-of-Fit	3	1.7195	0.5732	254.90	0.000
Pure Error	56	0.1259	0.0022		
Total	64	29.8111			

Model Summary

S	R-sq	R-sq(adj)	R-sq(pred)
0.176855	93.81%	93.29%	91.94%

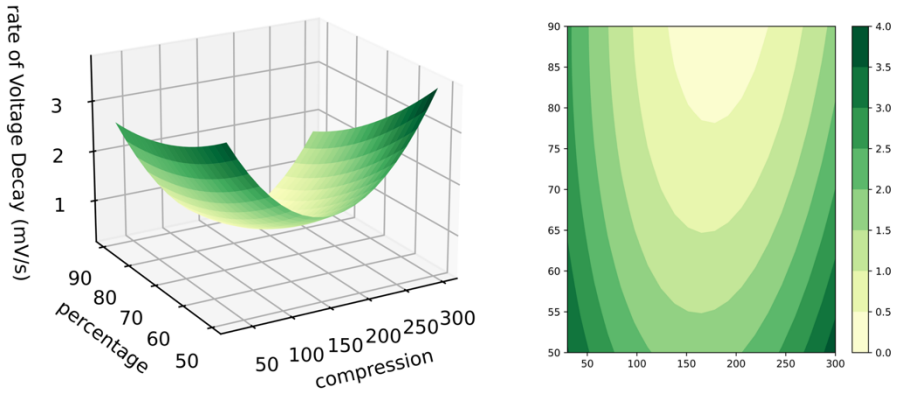


Fig. 38: Voltage Decay a) ANOVA table, b) Regression table, c) surface plot, d) contour plot

6.3 Optimization of Graphite Composite Factors

Minitab has an optimization tool module that allows the precise identification of the optimal ratio and compression force. in the response surface for the power generated there were similar results. The highest power generation occurs at a graphite:PVAc ratio of 89% and a compression strength of 162N. Finally, the in, response surface for voltage decay, the optimal voltage decay value is minimized instead of maximized. The optimal voltage decay occurs at a graphite:PVAc ratio of 89% and a compression strength of 167N. From the optimization tool which can be found in appendix C optimizing across all three response variables results in a suggested graphite palette that uses a compression force of 165 N and a ratio of 89%.

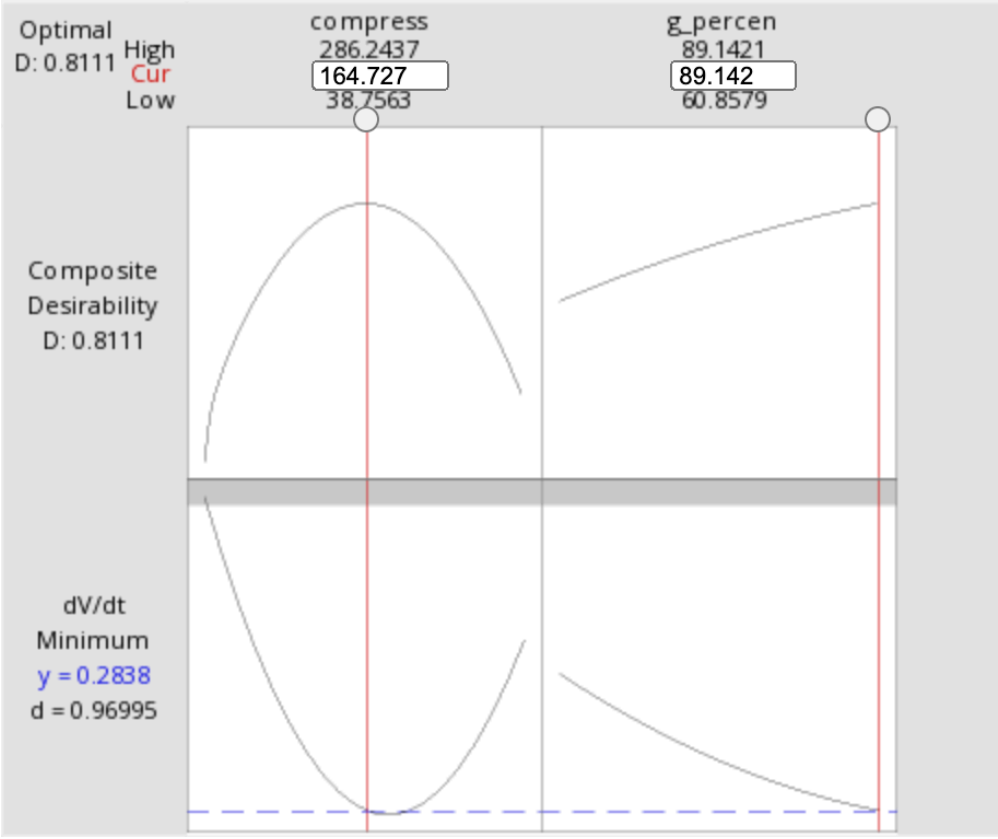


Fig. 39: Minitab optimization tool indicates what compression and graphite percentage would produce optimized maximum voltage, power output and voltage decay.

6.4 Summary

This chapter also analyzed a small-scale water-based power generation system. It looked at the effect of two material factors: compression force and the graphite pallette:PVAc ratio on three response variables: the maximum voltage generated in the system, the average power generated over 150 seconds, and the rate of decay of the voltage generated. This analysis covered DOE using central composite method, one-way ANOVA, analysis of residuals, the generation and analysis of a response surface and finally, a discussion of the real-world implications of this analysis.

Through this analysis, it was found that the response surfaces generated by the model were well fitted to the data, however there was also some level of lack of fit. One way analysis of variance and regression could well fit responses to the compression strength parameter, but poorly fit the IRL:PVAc ratio. Finally, the generated response surfaces were used to estimate the optimal conditions to create a graphite palette material that would maximize voltage and power generated and minimize voltage decay.

Chapter 7
Conclusions and Recommendations

7.1 Conclusions

There are 4 main conclusions that can be drawn from this work.

a. It seems as though powdered graphite or a conductive carbaceous material is essential to the ideal function of the sensor. This work elucidates the role of graphite in the sensor, which was previously thought to be solely a means for water to reach the magnesium surface. Through characterization of graphite in different states of use, it is apparent that graphite is affected by water absorption and drying. This change is apparent in changes in surface hydrophobicity, as well as in a decrease of oxygen content, as demonstrated through EDX, Raman, and XPS. Additionally, it is demonstrated that Mg ions are not deposited in the graphite at a significant rate, regardless of the length of the reaction.

b. In its practical use, the sensor would have to withstand certain environmental conditions and continue to work. The sensor was able to function successfully across a range of temperatures, humidity levels, and electrolyte concentrations. Changing conditions did vastly alter sensor performance, however and the magnitude of these changes was determined so as to determine the overall sensitivity of the sensor to a range of environmental conditions.

c. The sensor aging and shelf life were examined. First an accelerated oxidation was tested in which the sensors' voltage output were shown to decrease as they were kept in more extreme oxidation conditions. Next a real time shelf-life test was conducted. The fluctuations in the sensor voltage were examined and seemed to change seasonally. This change was shown to follow changes in local humidity. It was shown already that the sensors are affected by elevated humidity.

d. A composite of graphite and polyvinyl acetate could be used to replace the delicate graphite powder palette. There was a demonstrated drop in voltage output associated with this composite piece so an ideal formulation was developed that would minimize negative side effects that arose from adding the PVAc binder to the graphite. This composite piece could be optimized across two inputs: ratio of PVA:graphite and compression force on the composite piece. Statistical analysis was used to optimize for 3 outputs: maximizing initial voltage, minimizing rate of voltage decay, and maximizing power output. The optimized inputs were 164N and 89% graphite in the composite.

7.2 Recommendations

Based on this work, a few recommendations for the study of the materials stack as well as for overall sensor design can be made.

a. The sensor was determined in Chapters 4 and 5 to be extremely sensitive to environmental conditions. These conditions did not necessarily cause the sensor to fail, however the small decline in sensor performance will likely affect the overall repeatability of the sensor. The materials in the sensor such as filter paper and graphite are absorbent, and magnesium is reactive. These qualities cause the sensor to oxidize and absorb water and age it faster. It may improve the sensor consistency and repeatability if the materials are protected from air or water.

b. The study on the graphite composite in this work showed that there was an effect on voltage and voltage drop caused by the PVAc composite. This may have been due to the decreased conductivity or absorbency of the graphite While the composite was successful in improving the resilience of the sensor, the decrease in electrical performance was significant. Further development of composite will be necessary to significantly scale up manufacturing without resulting in many sensor failures. It will be productive to attempt to create similar composite with other binders, or even to try a different approach of encasing the graphite in a porous polymeric foam.

c. The form factor of this sensor and its incorporation into a network will elevate the sensor into a more versatile and usable tool. The current morphology is similar to many point detectors on the market; however, it is clear with point detectors that they must be deployed at a high rate to protect an area. Incorporation of the main sensor technology into a rope sensor or a flat, flexible sensor will allow for it to be used in versatile applications and may allow users to cover an area more reliably.

References

[1] Hydroelectric Power Water Use completed," Hydroelectric Power Water Use | U.S. Geological Survey, https://www.usgs.gov/special-topics/water-science-school/science/hydroelectric-power-water-use (accessed Jun. 25, 2023).

[2] R. A. Hughes, "Switzerland spent 4 years and €2 billion on this 'water battery,'" euronews, https://www.euronews.com/green/2022/06/30/enormous-water-battery-in-switzerland-will-help-prevent-power-shortages (accessed Jun. 25, 2023).

[3] Northbridge Insurance, "Why water-monitoring technology is a game-changer for high-rise construction projects," 2022. https://www.theglobeandmail.com/business/adv/article-why- water-monitoring-technology-is-a-game-changer-for-high-rise/(accessed Jun. 25, 2023).

[4] "The best gear for Small Apartments," The New York Times, https://www.nytimes.com/wirecutter/reviews/best-gear-for-small-apartments/ (accessed Jun. 25, 2023).

[5] C. Hagerty, "When floods destroy homes, hidden costs can devastate survivors," The New York Times, https://www.nytimes.com/2023/04/22/business/flood-damage-home-costs.html (accessed Jun. 25, 2023).

[6] "What is an air barrier – vapor barrier – water resistive barrier?," What is an Air Barrier – Vapor Barrier – Water Resistive Barrier? > Carlisle Coatings and Waterproofing, https://www.carlisleccw.com/view.aspx?mode=post&contentID=43 (accessed Jun. 25, 2023).

[7] Flood and storm protection, https://www.ibc.ca/stay-protected/severe-weather-safety/flood-and-water (accessed Jun. 25, 2023).

[8] S. Hill, "The 5 best water leak detectors for your home," Wired, https://www.wired.com/gallery/best-water-leak-detectors/ (accessed Jun. 25, 2023).

[9] Enviromon.net, “Best practices for water leak and flood detection sensors,” Enviromon, https://www.enviromon.net/water-leak-flood-detection-sensors/ (accessed Jun. 25, 2023).

[10] D-Link, “DCH-S 63 Water Sensing Pod Specifications,” 2020. [Online]. Available: www.dlink.com

[11] Nowa, “Nowa Technical-Data-Sheet-NOWDSF300,” 20 6.

[12] Yo-Link, “YS7903 UC Water Leak Sensor,” 2022.

[13] Aqara, “Aqara Water Leak Sensor.” https://www.aqara.com/us/water_leak_sensor.html (accessed May 8, 2023).

[14] Govee, “Govee Water Leak Detector Product Guide and User Manual”.

[15] Centralite, “33 5-G Product Data Sheet,” 20 8. [Online]. Available: http://centralite.com

[16] Dome, “Leak Sensor User Manual DMWS .” [Online]. Available: www.domeha.com

[17] Orbit, “B-HYVE FLOOD SENSOR Instruction Manual.”

[18] Levi Nathan Johnston, “Integration of a Self-Powered Sensor and Electronics to Produce a Battery-Free, Wireless, Water Leak Detection Device,” MASc, University of Waterloo, Waterloo, 2022.

[19] Kamalpreet Kaur Kamalpreet Kaur, “Performance and Degradation of a Battery-Free Water Leak Detection Device,” MASc, University of Waterloo, Waterloo, 2022.

[20] “State of IOT 2023: Number of connected IOT devices growing 6% to 6.7 billion globally,” IoT Analytics, https://iot-analytics.com/number-connected-iot-devices/ (accessed Jun. 26, 2023).

[21] R. Huntley, “Energy harvesting: Powering IOT devices reliably and sustainably,” EE Times Europe, https://www.eetimes.eu/energy-harvesting-powering-iot-devices-reliably-and-sustainably/ (accessed Jun. 26, 2023).

[22] Bakker, “CMOS smart temperature sensors - an overview,” Proceedings of IEEE Sensors, 2002. doi: 0. 09/icsens.2002. 037330

[23] W. Babatain, S. Bhattacharjee, A. M. Hussain, and M. M. Hussain, “Acceleration sensors: Sensing Mechanisms, emerging fabrication strategies, materials, and applications,” ACS Applied Electronic Materials, vol. 3, no. 2, pp. 504–53 , 202 . doi: 0. 02 /acsaelm.0c00746

[24] “Gyro sensors: Technology,” Epson, https://corporate.epson/en/technology/search-by-products/microdevice/gyro-sensor.html (accessed Jun. 26, 2023).

[25] R. PCB, “Working Principles of a touch sensor,” Printed Circuit Board Manufacturing & PCB Assembly - RayMing, https://www.raypcb.com/touch-sensor/ (accessed Jun. 26, 2023).

[26] S.-S. Je, T. Sharma, Y. Lee, B. Gill, and J. X. Zhang, “A thin-film piezoelectric PVDF-TRFE based implantable pressure sensor using lithographic patterning,” 20 IEEE 24th International Conference on Micro Electro Mechanical Systems, 20 . doi: 0. 09/memsys.20 .5734507

[27] L. Mennel et al., “Ultrafast Machine Vision with 2D material neural network image sensors,” Nature News, https://www.nature.com/articles/s4 586-020-2038-x/ (accessed Jun. 26, 2023).

[28] H. Landaluce et al., “A review of IOT sensing applications and challenges using RFID and Wireless Sensor Networks,” Sensors, vol. 20, no. 9, p. 2495, 2020. doi: 0.3390/s20092495

[29] R. Mitchell, “IOT in space: How tiny devices are making a huge impact,” , https://www.electropages.com/blog/2023/06/how-iot-can-help-astronomers-capture-meteors (accessed Jun. 26, 2023).

[30] M. Swan, “Sensor mania! the internet of things, wearable computing, objective metrics, and the quantified self 2.0,” MDPI, https://www.mdpi.com/2224-2708/ /3/2 7 (accessed Jun. 26, 2023).

[31] “Internet of things,” McKinsey & Company, https://www.mckinsey.com/featured-insights/internet-of-things/our-insights (accessed Jun. 26, 2023).

[32] “Flo: Smart home,” MOEN, https://www.moen.ca/flo (accessed Jun. 26, 2023).

[33] [0] “Pillar Technologies - the future of construction site risk management,” Recon Pillar LLC, https://pillar.tech/ (accessed Jun. 26, 2023).

[34] N. Iqbal, M. Masood, A. A. Nasir, and K. K. Qureshi, “Review of contemporary energy harvesting techniques and their feasibility in wireless geophones,” International Journal of Energy Research, vol. 46, no. 5, pp. 5703–5730, 2022. doi: 0. 002/er.7626

[35] C. Xu, Y. Song, M. Han, and H. Zhang, “Portable and wearable self-powered systems based on emerging energy harvesting technology,” Microsystems & Nanoengineering, vol. 7, no. , 202 . doi: 0. 038/s4 378-02 -00248-z

[36] Y. Kheng and S. Kumar, “Review of Energy Harvesting Technologies for sustainable WSN,” Sustainable Wireless Sensor Networks, 20 0. doi: 0.5772/ 3062

[37] M. K. Mishu et al., “Prospective efficient ambient energy harvesting sources for IOT-equipped sensor applications,” Electronics, vol. 9, no. 9, p. 345, 2020. doi: 0.3390/electronics909 345

[38] D. Hoffmann et al., “Energy harvesting from fluid flow in water pipelines for smart metering applications,” Journal of Physics: Conference Series, vol. 476, p. 0 2 04, 20 3. doi: 0. 088/ 742-6596/476/ /0 2 04

[39] “Vibration Energy Harvesting,” Harnessing Bistable Structural Dynamics, pp. 8 –290, 20 7. doi: 0. 002/978 9 28052.ch4

[40] J. Curry, N. Harris, and N. White, “A tuneable pressure-based energy harvester for powering the environmental internet of things,” Micromachines, vol. 3, no. , p. 973, 2022. doi: 0.3390/mi 3 973

[41] G. Lee et al., “Piezoelectric energy harvesting using mechanical metamaterials and phononic crystals,” Communications Physics, vol. 5, no. , 2022. doi: 0. 038/s42005-022-00869-4

[42] L.-G. Tran, H.-K. Cha, and W.-T. Park, “RF Power Harvesting: A review on designing methodologies and applications,” Micro and Nano Systems Letters, vol. 5, no. , 20 7. doi: 0. 86/s40486-0 7-005 -0

[43] “Thermal energy harvesting,” Strano Research Group, https://srg.mit.edu/thermal/ (accessed Jun. 26, 2023).

[44] L. E. Helseth, “Harvesting energy from light and water droplets by covering photovoltaic cells with transparent polymers,” Applied Energy, vol. 300, p. 7394, 202 . doi: 0. 0 6/j.apenergy.202 . 7394

[45] C. Xu, Y. Song, M. Han, and H. Zhang, “Portable and wearable self-powered systems based on emerging energy harvesting technology,” Microsystems & Nanoengineering, vol. 7, no. , 202 . doi: 0. 038/s4 378-02 -00248-z

[46] [ ] E. Kandahari, E. J. Smith, and J. C. Goeltz, “Beyond the textbook: Introducing undergraduates to Practical Electrochemistry,” Journal of Chemical Education, vol. 98, no. 0, pp. 3263–3268, 202 . doi: 0. 02 /acs.jchemed. c00 55

[47] [0] Organic Redox Chemistry, 202 . doi: 0. 002/97835278 5678

[48] G. Krishnan, Standard red potentials, https://users.stlcc.edu/gkrishnan/electrochem2.html (accessed Jun. 26, 2023).

[49] Electrochemistry, https://xaktly.com/Electrochemistry.html (accessed Jun. 26, 2023).

[50] Electrochemical cells, http://hyperphysics.phy-astr.gsu.edu/hbase/Chemical/electrochem.html (accessed Jun. 26, 2023).

[51] E.-M. Yang, T. J. Greenbowe, and T. Andre, “The effective use of an interactive software program to reduce students’ misconceptions about batteries,” Journal of Chemical Education, vol. 8 , no. 4, p. 587, 2004. doi: 0. 02 /ed08 p587

[52] K. Schmidt-Rohr, “How batteries store and release energy: Explaining basic electrochemistry,” Journal of Chemical Education, vol. 95, no. 0, pp. 80 – 8 0, 20 8. doi: 0. 02 /acs.jchemed.8b00479

[53] H. Berg, Batteries for Electric Vehicles: Materials and Electrochemistry. Cambridge, United Kingdom: Cambridge University Press, 20 5.

[54] “Fuel cells,” Energy.gov, https://www.energy.gov/eere/fuelcells/fuel-cells (accessed Jun. 26, 2023).

[55] R. J. Lim et al., “A review on the electrochemical reduction of CO2 in fuel cells, metal electrodes and molecular catalysts,” Catalysis Today, vol. 233, pp. 69– 80, 20 4. doi: 0. 0 6/j.cattod.20 3. .037

[56] M. C. Tucker, “Progress in metal-supported solid oxide fuel cells: A Review,” Journal of Power Sources, vol. 95, no. 5, pp. 4570–4582, 20 0. doi: 0. 0 6/j.jpowsour.20 0.02.035

[57] Q. Sun et al., “Recent advances in solid-state metal–Air Batteries,” Carbon Energy, vol. 5, no. 2, 2022. doi: 0. 002/cey2.276

[58] Agrawal and C. M. Hussain, “Wearable Metal-Air Batteries,” Metal-Air Batteries, pp. 335–346, 2023. doi: 0. 20 /978 00329576 -23

[59] Y. Li and J. Lu, “Metal–air batteries: Will they be the future electrochemical energy storage device of choice?,” ACS Energy Letters, vol. 2, no. 6, pp. 370– 377, 20 7. doi: 0. 02 /acsenergylett.7b00 9

[60] M.-S. Park et al., “Porous nanoarchitectures of spinel-type transition metal oxides for Electrochemical Energy Storage Systems,” Physical Chemistry Chemical Physics, vol. 7, no. 46, pp. 30963–30977, 20 5. doi: 0. 039/c5cp05936d

[61] D. Ahuja, V. Kalpna, and P. K. Varshney, “Metal Air Battery: A sustainable and low cost material for energy storage,” Journal of Physics: Conference Series, vol. 9 3, no. , p. 0 2065, 202 . doi: 0. 088/ 742-6596/ 9 3/ /0 2065

[62] J. Zhang, Q. Zhou, Y. Tang, L. Zhang, and Y. Li, “Zinc–Air Batteries: Are they ready for prime time?,” Chemical Science, vol. 0, no. 39, pp. 8924–8929, 20 9. doi: 0. 039/c9sc0422 k

[63] R. Ma et al., “A review of oxygen reduction mechanisms for metal-free carbon-based electrocatalysts,” npj Computational Materials, vol. 5, no. , 20 9. doi: 0. 038/s4 524-0 9-02 0-3

[64] J. Feng et al., “High-performance magnesium–carbon nanofiber hygroelectric generator based on interface-mediation-enhanced capacitive discharging effect,” ACS Applied Materials & Interfaces, vol. 2, no. 2 , pp. 24289–24297, 2020. doi: 0. 02 /acsami.0c04895

[65] “Magnesium,” Tech Steel & Materials, https://www.techsteel.net/alloy/magnesium (accessed Jun. 26, 2023).

[66] F. Z. Corporation et al., “Magnesium AZ3 B alloy (UNS M 3),” AZoM.com, https://www.azom.com/article.aspx?ArticleID=6707 (accessed Jun. 26, 2023).

[67] D. J. Wetzel et al., “Passivation dynamics in the anisotropic deposition and stripping of bulk magnesium electrodes during electrochemical cycling,” ACS Applied Materials & Interfaces, vol. 7, no. 33, pp. 8406– 84 4, 20 5. doi: 0. 02 /acsami.5b04487

[68] F. Alharbi, A. A. Abahussain, M. H. Nazir, and S. Z. Zaidi, “A high-energy-density magnesium-air battery with nanostructured polymeric electrodes,” Polymers, vol. 4, no. 5, p. 3 87, 2022. doi: 0.3390/polym 4 53 87

[69] P. Xie, M. Z. Rong, and M. Q. Zhang, “Moisture Battery formed by direct contact of magnesium with foamed polyaniline,” Angewandte Chemie, vol. 28, no. 5, pp. 837–84 , 20 5. doi: 0. 002/ange.20 5 0686

[70] H. ZHAO, P. BIAN, and D. JU, “Electrochemical performance of magnesium alloy and its application on the Sea Water Battery,” Journal of Environmental Sciences, vol. 2 , 2009. doi: 0. 0 6/s 00 -0742(09)60045-0

[71] K. Chandrasekhar, “Effective and nonprecious cathode catalysts for oxygen reduction reaction in microbial fuel cells,” Microbial Electrochemical Technology, pp. 485–50 , 20 9. doi: 0. 0 6/b978-0-444-64052-9.000 9-4

[72] L. Gan, H. Du, B. Li, and F. Kang, “Surface-reconstructed graphite nanofibers as a support for cathode catalysts of fuel cells,” Chemical Communications, vol. 47, no. 3, p. 3900, 20 . doi: 0. 039/c cc 0 79j

[73] J.-M. André and G. Leroy, “Electronic structure of graphite,” International Journal of Quantum Chemistry, vol. 3, no. 6, pp. 983–999, 969. doi: 0. 002/qua.5600306 8

[74] “Graphene oxide,” ACS MATERIAL, https://www.acsmaterial.com/blog-detail/graphene-oxide.html (accessed Jun. 26, 2023).

[75] T. Agency, “Structure and properties - flake graphite,” Flake Graphite: Properties and Structure | Tirupati Graphite, https://tirupatigraphite.co.uk/structure-and-properties/ (accessed Jun. 26, 2023).

[76] J. Asenbauer et al., “The success story of graphite as a lithium-ion anode material – fundamentals, remaining challenges, and recent developments including silicon (oxide) composites,” Sustainable Energy & Fuels, vol. 4, no. , pp. 5387–54 6, 2020. doi: 0. 039/d0se00 75a

[77] W. V. Zyl, “Analysis of graphite for lithium-ion batteries,” Advancing Materials, https://www.thermofisher.com/blog/materials/analysis-of-graphite-for-lithium-ion-batteries/ (accessed Jun. 26, 2023).

[78] U. 20 2022, “Are graphene batteries the future?,” AZoNano.com, https://www.azonano.com/article.aspx?ArticleID=6233 (accessed Jun. 26, 2023).

[79] Simanjuntak, R. Siburian, H. Marpaung, and Tamrin, “Properties of mg/graphite and MG/graphene as cathode electrode on primary cell battery,” Heliyon, vol. 6, no. , 2020. doi: 0. 0 6/j.heliyon.20 9.e03 8

[80] J. Li, D. Song, K. Du, Z. Wang, and C. Zhao, “Performance of graphite felt as a cathode and anode in the electro-fenton process,” RSC Advances, vol. 9, no. 66, pp. 38345–38354, 20 9. doi: 0. 039/c9ra07525a

[81] Y. Leng, Materials characterization: Introduction to Microscopic and Spectroscopic Methods, 2nd ed. Weinheim: Wiley, 20 3.

[82] "Reduce Charging in SEM Using Low Voltage Imaging - Nanoscience Instruments", Nanoscience Instruments, 202 . [Online]. Available: https://www.nanoscience.com/applications/materials-science/reduce-charging-in-sem-using-low- voltage-imaging/. [Accessed: 7- Jul- 202].

[83] “Raman,” Chemical Analysis, Life Sciences, and Diagnostics, https://www.agilent.com/en/support/molecular-spectroscopy/raman-spectroscopy/what-is-raman-spectroscopy-faq-guide (accessed Jun. 26, 2023).

[84] Raman analysis, https://www.intertek.com/analysis/raman/ (accessed Jun. 26, 2023)

[85] .-M. Yang, T. J. Greenbowe, and T. Andre, “The effective use of an interactive software program to reduce students’ misconceptions about batteries,” Journal of Chemical Education, vol. 8 , no. 4, p. 587, 2004. doi: 0. 02 /ed08 p587

[86] “Carbon: XPS periodic table: Thermo fisher scientific - US,” XPS Periodic Table | Thermo Fisher Scientific - US, https://www.thermofisher.com/ca/en/home/materials-science/learning-center/periodic-table/non-metal/carbon.html (accessed Jun. 10, 2023).

[87] Q. Chu *et al.*, “Volumetric enhancement of Raman scattering for fast detection based on a silver-lined hollow-core fiber,” *Optics Express*, vol. 27, no. 7, p. 10370, 2019. doi:10.1364/oe.27.010370

[88] N. A. M. Noor, S. K. Kamarudin, M. Darus, N. F. D. Yunos, and M. A. Idris, "Photocatalytic properties and graphene oxide additional effects in tio2," *Solid State Phenomena*, vol. 280, pp. 65–70, 2018. doi:10.4028/www.scientific.net/ssp.280.65

[89] V. Zólyomi, J. Koltai, and J. Kürti, "Resonance raman spectroscopy of graphite and graphene," *physica status solidi (b)*, vol. 248, no. 11, pp. 2435–2444, 2011. doi:10.1002/pssb.201100295

[90] R. PCB, "How the shelf life of electronic components impacts performance in electronic devices," Printed Circuit Board Manufacturing & PCB Assembly - RayMing, https://www.raypcb.com/shelf-life-of-electronic-components/ (accessed Jun. 10, 2023).

[91] M. N. Haouet *et al.*, "Experimental accelerated shelf life determination of a ready-to-eat processed food," *Italian Journal of Food Safety*, vol. 7, no. 4, 2019.

[92] "Recent monthly Weather Records for kitchener-waterloo," Amateur Weather Statistics for Kitchener-Waterloo, Ontario, https://kitchenerwaterloo.weatherstats.ca/records_monthly.html (accessed Feb. 2, 2023).

[93] M. Á. Rodríguez-Valverde and M. Tirado Miranda, "Derivation of jurin's law revisited," *European Journal of Physics*, vol. 32, no. 1, pp. 49–54, 2010. doi:10.1088/0143-0807/32/1/005

[94] J. M. Montes, F. G. Cuevas, and J. Cintas, "Analytical theory for the description of powder systems under compression," *Applied Physics A*, vol. 99, no. 4, pp. 751–761, 2010. doi:10.1007/s00339-010-5682-4

[95] Getting started with Minitab Statistical Software, https://www.minitab.com/content/dam/www/en/uploadedfiles/documents/getting-started/MinitabGettingStarted_EN.pdf (accessed Jul. 10, 2023).